UNIVERSIDADE FEDERAL DE MINAS GERAIS

Escola de Engenharia

Programa de Pós-graduação em Engenharia Metalúrgica, Materiais e de Minas

Victor Cagnoni Jakitsch

OBTAINING AL-CU-FE PARTICLES WITH A CU-RICH SKELETAL SURFACE FOR CATALYTICAL APPLICATIONS

Belo Horizonte

2022

Victor Cagnoni Jakitsch

OBTAINING AL-CU-FE PARTICLES WITH A CU-RICH SKELETAL SURFACE FOR CATALYTICAL APPLICATIONS

Dissertation submitted to the Programa de Pós-Graduação em Engenharia Metalúrgica, Materiais e de Minas from the Escola de Engenharia da Universidade Federal de Minas Gerais, as a partial requirement for obtaining a master's degree in Metallurgical, Materials and Mining Engineering.

Advisor: Prof. Witor Wolf
Co-Advisor: Prof. Eduardo Nunes

Belo Horizonte

2022

Victor Cagnoni Jakitsch

FABRICAÇÃO DE PARTÍCULAS DE AL-CU-FE COM UMA SUPERFÍCIE ESQUELETAL RICA EM COBRE PARA APLICAÇÕES CATALÍTICAS

Dissetação apresentada ao Programa de Pós-Graduação em Engenharia Metalúrgica, Materiais e de Minas da Escola de Engenharia da Universidade Federal de Minas Gerais, como requisito parcial para obtenção do Grau de Mestre em Engenharia Metalúrgica, Materiais e de Minas.

Orientador: Prof. Witor Wolf
Co- Orientador: Prof. Eduardo Nunes

Belo Horizonte

2022

UNIVERSIDADE FEDERAL DE MINAS GERAIS
ESCOLA DE ENGENHARIA
Programa de Pós-Graduação em Engenharia
Metalúrgica, Materiais e de Minas

A dissertação intitulada "Obtaining Al-Cu-Fe Particles with a Cu-rich Skeletal Surface for Catalytical Applications", área de concentração: Metalurgia Física e de Transformação, apresentada pelo candidato Victor Cagnoni Jakitsch, para obtenção do grau de Mestre em Engenharia Metalúrgica, Materiais e de Minas, foi aprovada pela comissão examinadora constituída pelos seguintes membros:

Dr. Witor Wolf
Orientador (UFMG)

Dr. Eduardo Henrique Martins Nunes
Coorientador (UFMG)

Dr. Breno Rocha Barrioni
(UFVJM)

Dr. Claudemiro Bolfarini
(UFSCar)

Coordenador do Programa de Pós-Graduação em
Engenharia Metalúrgica, Materiais e de Minas/UFMG

Belo Horizonte, 13 de outubro de 2022

DEDICATÓRIA

Aos meus pais

AGRADECIMENTOS

Aos meus pais e meu irmão pelo apoio durante o período de elaboração deste trabalho.

À Mara por estar sempre presente e pelo apoio.

Ao meu orientador Professor Witor Wolf, pelo direcionamento, apoio e suporte durante esse período.

Ao meu coorientador Professor Eduardo Nunes, pelas discussões, suporte e ajuda na elaboração deste trabalho.

À MM Associados por ter permitido que eu me dedicasse à elaboração deste trabalho.

Aos colegas de laboratório pelas discussões e auxílio.

À UFMG e ao Departamento de Engenharia Metalúrgica pela infraestrutura disponibilizada para que esse trabalho pudesse ser elaborado.

A todos aqueles que de alguma forma contribuíram para a elaboração desse trabalho.

I like the scientific spirit — the holding off, the being sure but not too sure, the willingness to surrender ideas when the evidence is against them: this is ultimately fine — it always keeps the way beyond open — always gives life, thought, affection, the whole man, a chance to try over again after a mistake — after a wrong guess.

(Walt Whitman)

ABSTRACT

The expansion of the understanding horizon of quasicrystals relies, not only in its crystallographic and physical study, but also its applications. Following the last decades of investigation of different properties and possible applications of quasicrystals, this study used a quasicrystalline alloy powder of the Al-Fe-Cu system as catalyst for the degradation of the organic dye, Congo Red. The absence of studies that deeply evaluate these properties, alongside the pressing environmental issue of water pollutant control, make this material an alternative to perform the removal of these type of substances from industrial effluents. In this study, an $Al_{62.5}Cu_{25}Fe_{12.5}$ (%at.) alloy was fabricated by gas-atomization, following a leaching procedure of the quasicrystal-based powder in an alkaline solution aiming to remove aluminium atoms from the surface, exposing the Cu-rich phase. The micro and nanometric Cu-rich particles are the ones responsible for the catalytic effect in theses reactions. The gas-atomized and leached powder were microstructurally characterized using several techniques. The Congo Red decomposition, due to the presence of the leached particles was monitored by Ultraviolet Spectroscopy. The results indicate that the $Al_{62.5}Cu_{25}Fe_{12.5}$ microstructure, composed initially by icosahedral quasicrystals and the τ-AlCu(Fe) phases, developed a skeletal structure where most of the quasicrystals from the particle´s surface were removed while the τ -AlCu(Fe) phase was mostly preserved as it was found in the atomized particles. The presence of this phase at the particle´s surface, provided optimal locations for the Congo Red molecules to interact with the Cu rich phase.

Keywords: Quasicrystals; Catalysis; Congo Red.

RESUMO

A expansão do horizonte de compreensão dos quasicristais depende, não apenas de seu estudo cristalográfico e físico, mas também de suas aplicações. Após as últimas décadas de investigação de diferentes propriedades e possíveis aplicações dos quasicristais, este estudo utilizou um pó de liga quasicristalina do sistema Al-Fe-Cu como catalisador para a degradação da tintura orgânica, Vermelho Congo. A ausência de estudos que avaliem profundamente estas propriedades, juntamente com a premente questão ambiental do controle de poluentes da água, fazem deste material uma alternativa para realizar a remoção deste tipo de substâncias de efluentes industriais. Neste estudo, uma liga $Al_{62.5}Cu_{25}Fe_{12.5}$ (%at.) foi fabricada por atomização a gás, seguindo um procedimento de lixiviação do pó à base de quasicristal numa solução alcalina com o objetivo de remover átomos de alumínio da superfície, expondo as partículas ricas em cobre. As partículas ricas em cobre micro e nanométricas são as responsáveis pelo efeito catalítico nestas reações. O pó atomizado e lixiviado teve sua microestrutura caracterizada utilizando diversas técnicas. A decomposição do vermelho Congo, devido à presença das partículas lixiviadas, foi monitorada por Espectroscopia Ultravioleta. Os resultados indicam que a microestrutura $Al_{62.5}Cu_{25}Fe_{12.5}$, composta inicialmente por quasicristais icosaédricos e as fases τ-AlCu(Fe), desenvolveu uma estrutura esquelética onde a maioria dos quasicristais da superfície da partícula foi removida enquanto que a fase τ-AlCu(Fe) foi preservada em sua maioria como foi encontrada nas partículas atomizadas. A presença desta fase na superfície da partícula, forneceu locais ideais para que as moléculas de Vermelho Congo interagissem com a fase rica em Cu.

Palavras-chave: Quasicristais; Catálise; Vermelho Congo.

FIGURES SUMMARY

SUMMARY TABLES

List of abriviations and symbols

BET   Brunauer-Emmett-Teller analysis

BOO   Bond Orientation Order

CMA   Complex Metallic Alloys

CR   Congo Red

DTA   Differential Thermal Analysis

EDS   Energy-Dispersive X-ray Spectroscopy

EELS   Electron Energy Loss Spectroscopy

ESI (–)–MS   Electrospray Ionization Mass Spectrometry in the negative ion mode

GC–MS   Gas Chromatography–Mass Spectrometry

IUPAC   International Union of Pure and Applied Chemistry

QC   Quasicrystal

SAED   Selected Area Electron Diffraction

SEM   Scanning Electron Microscopy

SRM   Steam Reforming of Methanol

TEM   Transmission Electrion Microscopy

XRD   X-Ray Diffraction

SUMMARY

1 INTRODUCTION

Quasicrystalline materials were first documented by Dan Shechtman in 1984 [1] in a laboratory environment using rapid solidified Al alloys. Other occurrences, outside of controlled production, were lately identified sites of extreme events, such as atomic bomb detonation and meteors [2,3]. Since its discovery, quasicrystals have been evaluated over its functional properties, and as it is a recent discovery, when compared to more stablished alloys such as steel, aluminium, and brass, much remains to be explored.

In the last decades, the catalytic properties of quasicrystal have attracted interest as an alternative catalyst for steam reforming of methanol for hydrogen production. Current energy and environmental concerns bring quasicrystals back as a not thoroughly explored material with interesting properties that may help tackle the challenges ahead. Still regarding the environmental opportunities of application of quasicrystal as catalysts, the degradation of organic pollutants is an area to be investigated. To the best of the author´s knowledge, there is only one study, concerning degradation of methylene blue, that proposed the use of quasicrystals for that end [4].

With a lack of studies on the application of quasicrystalline alloys in the degradation of organic dyes this study aims to evaluate the catalytic activity of $Al_{62.5}Cu_{25}Fe_{12.5}$ (%at.) to decompose Congo Red, after different leaching times. The powder material was characterized using scanning and transmission electron microscopy (SEM and TEM), X-ray diffraction (XRD), gas adsorption (BET) and Ultraviolet Spectroscopy (UV-Vis) analysis was used for monitoring the Congo Red decomposition rate.

1   INTRODUÇÃO

Materiais quasicristalinos foram documentados pela primeira vez por Dan Shechtman em 1984 [1] em um ambiente de laboratório usando ligas Al rapidamente solidificadas. Outras ocorrências, fora da produção controlada, foram recentemente identificadas locais de eventos extremos, tais como detonação de bombas atômicas e meteoros [2,3]. Desde sua descoberta, os quasicristais foram avaliados sobre suas propriedades funcionais, e como se trata de uma descoberta recente, quando comparada com ligas mais estáveis como aço, alumínio e latão, ainda há muito a ser explorado.

Nas últimas décadas, as propriedades catalíticas dos quasicristais atraíram o interesse como catalisador alternativo para a reforma a vapor do metanol para a produção de hidrogênio. As atuais preocupações energéticas e ambientais trazem os quasicristais de volta como um material não explorado completamente, com propriedades interessantes que podem ajudar a enfrentar os desafios do futuro. Ainda em relação às oportunidades ambientais de aplicação de quasicristais como catalisadores, a degradação de poluentes orgânicos é uma área a ser investigada. Tanto quanto é do conhecimento do autor, há apenas um estudo, referente à degradação do azul de metileno, que propôs o uso de quasicristais para esse fim [4].

Com a falta de estudos sobre a aplicação de ligas quasicristalinas na degradação de corantes orgânicos, este estudo visa avaliar a atividade catalítica do $Al_{62,5}Cu_{25}Fe_{12,5}$ (%at.) para decompor o Vermelho Congo, depois de diferentes tempos de lixiviação. O material em pó foi caracterizado utilizando microscopia eletrônica de varredura e transmissão (MEV e MET), difração de raios X (DRX), adsorção de gás (BET) e análise por espectroscopia ultravioleta (UV-Vis) para monitorar a taxa de decomposição do Vermelho Congo.

2 OBJECTIVES

2.1. General Objective

This study has as general objective evaluate the catalytic performance of a $Al_{62.5}Cu_{25}Fe_{12.5}$ (%at.) quasicrystalline powder alloy, before and after leaching, on organic dye decomposition.

2.2. Specific Objective

- Characterize the microstructure of the alloy before and after the leaching procedure to correlate their features to the catalytic properties.
- Use MEV to evaluate the morphology and phase changes before and after leaching.
- Measure pore size changes before and after leaching.
- Study the catalytic performance of the quasicrystal powder for Congo Red decomposition.

3   LITERATURE REVIEW

3.1. Crystals

The word crystal itself derives from the Greek word "*krystallos*", which means "ice", which is indeed crystalline, although not every crystalline material is ice. It is stated that the term was used figuratively to describe rock formations as quartz crystals, which in their turn resemble ice [5].

Crystals are broadly defined in crystallography as an anisotropic, homogeneous, three-dimensional periodic ordering of atoms, which are time-invariant [5–8]. The periodic nature of crystals mean that they can be summarized to a unitary entity that is repeated in the three special directions, which is called unit cell.

Crystals must obey rules that are used to distinguish the different crystalline structures that exist in nature. These rules regard the lattice structure and symmetry that the crystals exhibit. There are seven types of primitive lattice, which through changes in its centering allow for another seven types, as in Figure 3.1. The reason why there are only 14 types of Bravais lattices is because some of them are redundant i.e., they transform in one of the 14 lattices, and because to not all kinds of centering exists for all crystal systems due to symmetry [5,7].

The symmetry in crystals is used to describe the crystal class, which are derived from the 14 Bravais lattices, with a total of 32 crystal classes – crystallographic point groups. Symmetry can arise from different kinds of elements, such as identity, mirroring, rotation (2-, 3-, 4-, or 6-fold), inversion and rotoinversion [5].

By adding the previously mentioned symmetry elements with translational elements (glide reflection and screw rotation) the permutation of these elements produces 230 spatial groups, when chirality is also considered. They are also classified according to the 7 crystal systems discussed previously.

These being defined as the set of symmetry elements – with their symmetry operations – that completely describes the arrangement of a three-dimensional periodic pattern [5,6].
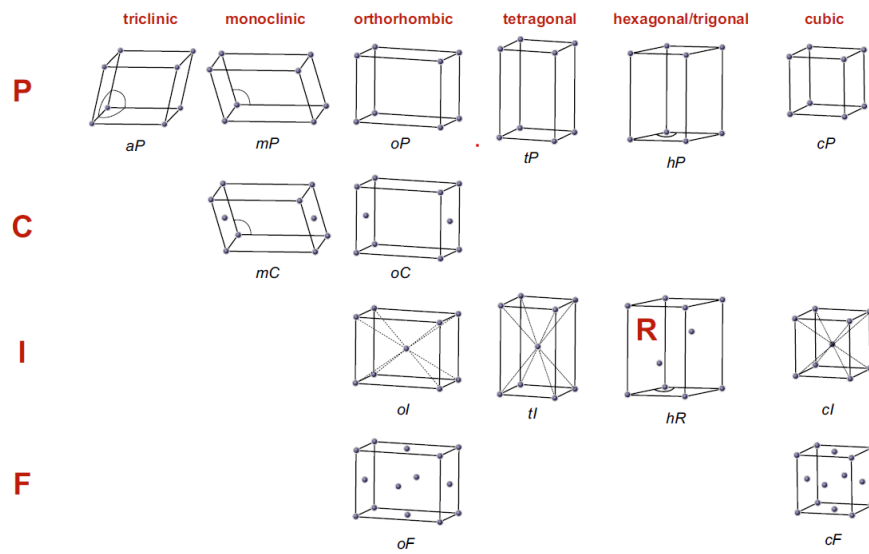
Figure 3.1 – The 14 Bravais lattices [5].

3.2. Quasicrystals

3.2.1. History

In the 70's and 80's, prior to the discovery of the first quasicrystal, mathematical research emerged regarding different types of tessellations, which basically mean, to cover a plane with no gaps or overlaps using defined and repeatable patterns. In 1974, Roger Penrose came up with a pentagonal pattern of arbitrary size, that could cover the entire plane. The pattern, however, is governed by purely local rules, and never repeats itself, forming a non-periodical tessellation, as in Figure 3.2.
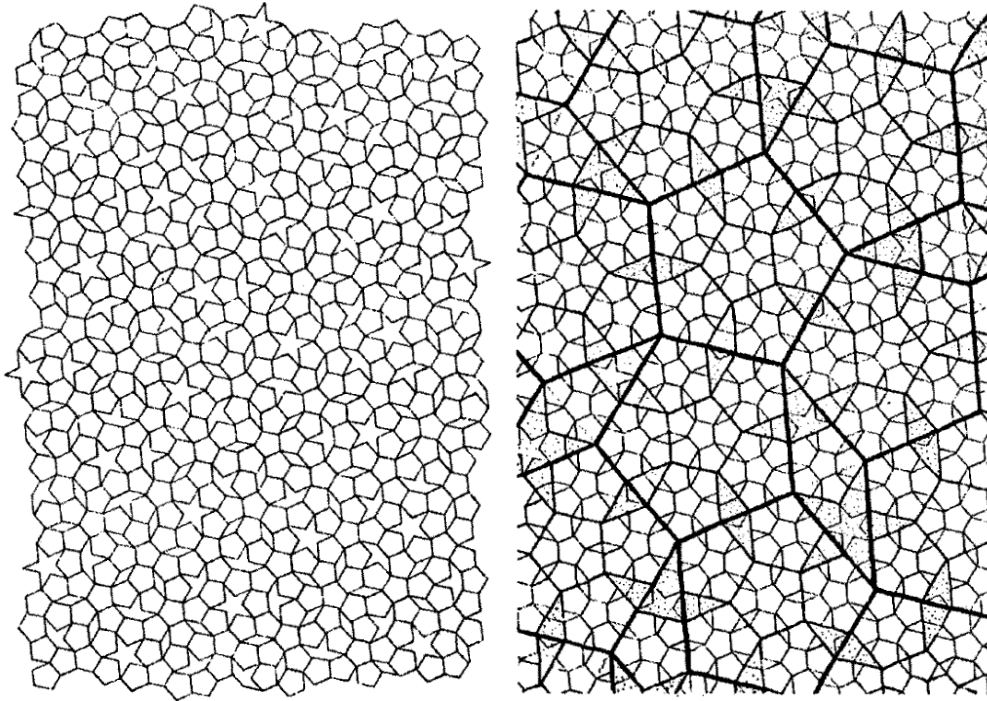
Figure 3.2 – Tessellation pattern using pentagon, five-pointed star, a kind of three-pointed star and a diamond, as their tilling shapes. Also, possible to be achieved by Inflation/deflation of the pattern into itself [9].

To make the pattern, four base shapes were used: pentagon, five-pointed star, a kind of three-pointed star and a diamond. The rules by which the entire plane is constructed can be enforced by adding motifs to the previous four shapes and expanding them to six different shapes, as there are now three pentagons, shown in Figure 3.3. It should also be noted that the pattern can be constructed by inflation or deflation of the base shape in or out of itself, as shown in Figure 3.2.
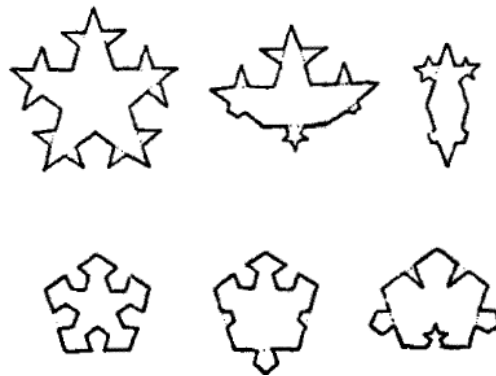
Figure 3.3 – Modified base shapes for placement rule enforcement with motifs [9].

Following Penrose, in the early 80's de Bruijn published a three papers series that investigate tessellation planes based on Penrose tiling [9]. In the first of those papers de Bruijn

stared with sequencies of zeros and ones using inflation and deflation rules, like those applied by Penrose, but on a single dimension. These rules were $1 \rightarrow 100$ and $0 \rightarrow 10$, meaning that from a starting sequence the following one would be constructed by replacing the current number by those indicated in the rules, applying these rules a sequency, which first term is 1, evolves as follows:

$$p_0 = 1$$
$$p_1 = 100$$
$$p_2 = 1001010$$
$$p_3 = 10010101001010010$$

… … … … … … … … … … …

De Bruijn also proposes equations which allow to produce sequences where indefinitely predecessors are obtained, these equations are shown below:

Let α and γ be reals, α > 1. Define sequences p, q by

$$p(z) = \lceil \gamma + (z + 1)/\alpha \rceil - \lceil \gamma + z/\alpha \rceil (z \in \mathbb{Z}) \qquad 3.1$$

$$q(z) = \lfloor \gamma + (z + 1)/\alpha \rfloor - \lfloor \gamma + z/\alpha \rfloor (z \in \mathbb{Z}) \qquad 3.2$$

With α being calculated from the equation below, in which d is a non-negative integer.

$$\alpha = \left(\left(\frac{1}{2}d + \frac{1}{2} \right)^2 + 1 \right)^{1/2} + \frac{1}{2}(d + 1)(z \in \mathbb{Z}) \qquad 3.3$$

He further highlights that in the case in which $d = 0$, $\alpha = \frac{1}{2}(\sqrt{5} + 1)$, leads to the production rule $1 \rightarrow 10$, $0 \rightarrow 1$, which is somewhat similar to the example shown previously. After creating a set of rules to produce infinite non periodic series, de Bruijn further investigated how to model the non-periodic Penrose tiling. In order not to get entangled into simply transcribing the equations and theorems used by de Bruijn to prove the general case for generation of non-periodical infinite series. Moving forward from one-dimension sequencies, as those discussed previously, to plane tessellations, more akin to those presented by Penrose.
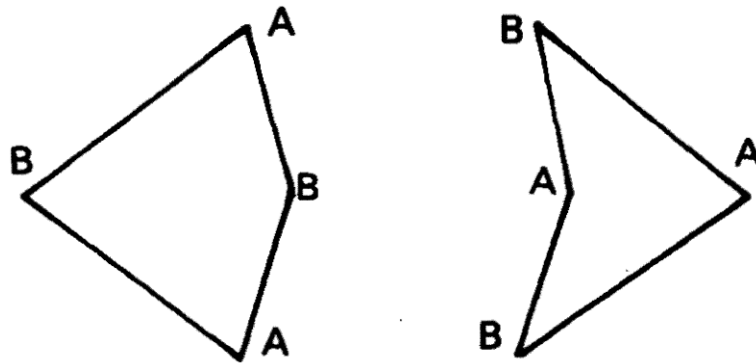
Figure 3.4 – Kite and dart geometries of tesselations.

This novel class of materials was first reported by Shechtman *et al.* in 1984 [1] followed shortly by Levine *et al.* [10]. Shechtman *et al.* [1] reported the existence of an experimentally produced metallic solid, working with rapidly cooled Al with 10-14at.% Mn, Fe or Cr alloys, which exhibited a point group symmetry $m\overline{3}\overline{5}$ (icosahedral), being a solid without translational order and long-range orientation order.
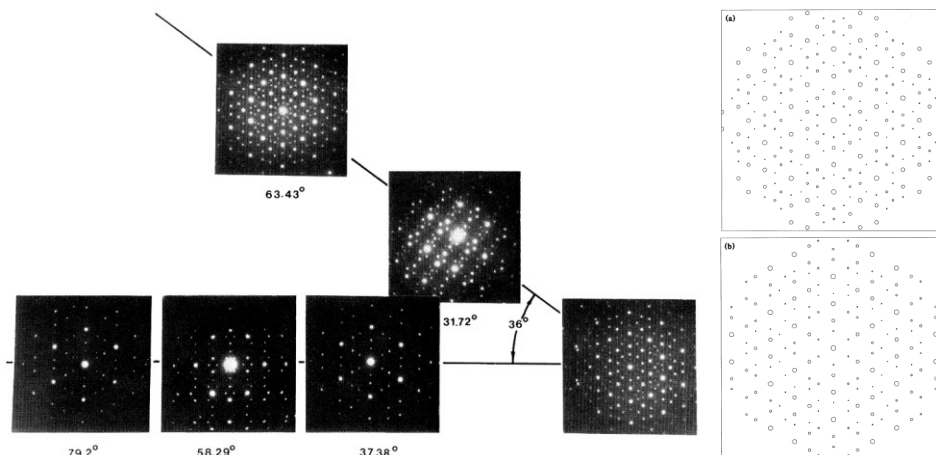
Figure 3.5 – Right: Selected-area electron diffraction patterns of an icosahedral phase [1]. Left: predicted diffraction pattern of an icosahedral quasicrystal [10].

Levine *et al.* [10] were conducting computer simulations of supercooled liquids and metallic glasses about 10% below the equilibrium melting temperature, in which icosahedral near neighbour bond orientation order (BOO) was observed. This suggested the possibility of a 3D state with a long-range icosahedral BOO but only short-range translational order. Levine went to further define quasicrystals as structures which are *quasiperiodic*. They also showed

that these new structures also display many properties of crystals, apart from its periodic nature or translational symmetry, which are lacking in the quasicrystals.

These shared properties do little to elucidate whether these novel discovered structures, the *quasicrystals*, are crystals or not, given that they lack the periodicity of crystals, while at the same time exhibit a defined diffraction pattern. To solve this conundrum the definition of crystals was updated by the International Union of Crystallography [11]. With a crystal being defined not only by its direct-space structure displaying on average long-range periodicity, but also by its reciprocal-space, in such way that a solid is a crystal if it has sharp diffraction peaks, which positions can be expressed by

$$\mathbf{H} = \sum_{i=1}^{n} h_i \boldsymbol{a}_i^* \ (n \geq 3) \qquad\qquad 3.4$$

Where $\boldsymbol{a}_i^*$ and h_i are the basis vectors of the reciprocal lattice and integer coefficients respectively, while *n* is the minimum for which the positions of the peaks can be described with the integer coefficient h_i. For conventional crystals, which are more abundant, *n=3*. The use of n>3, meaning higher dimensional analysis, is related to the indexing procedure for QCs, to do so it's usually used the Elser indexing scheme [12]. The mathematics behind this method is not further discussed here but the reader is encouraged to refer to the cited literature for a deeper explanation. An example of the results of this indexing scheme and of diffraction of quasicrystals is shown in Figure 3.6.
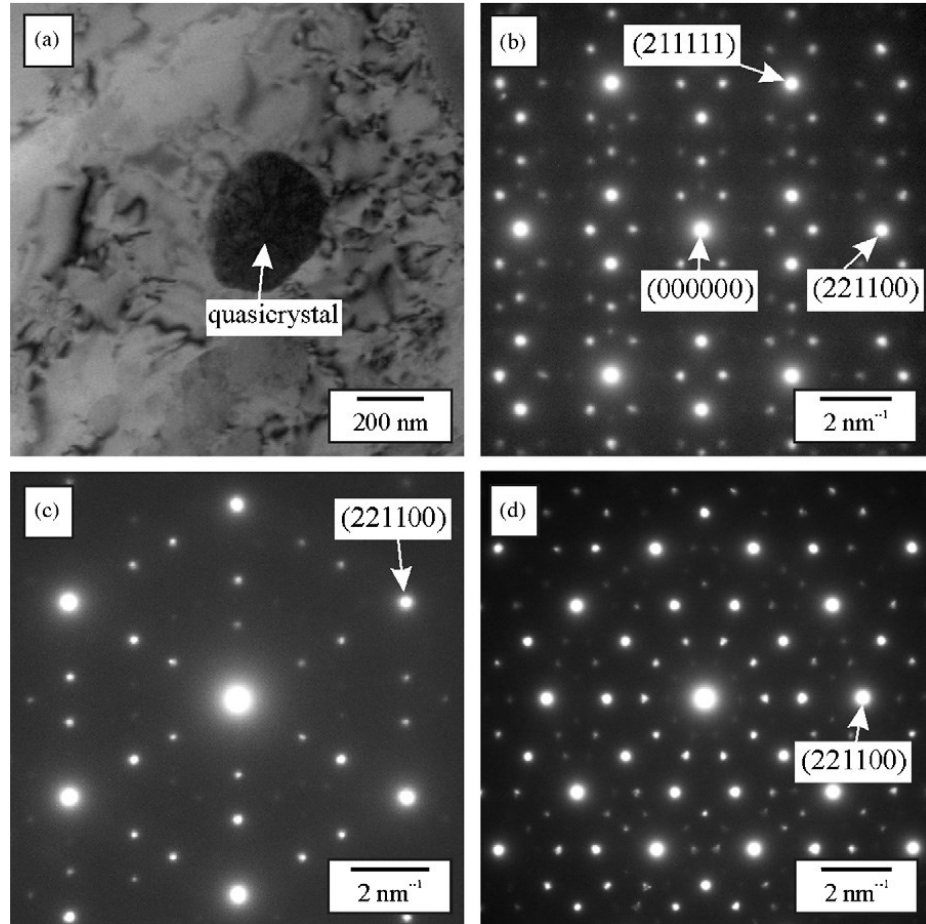
Figure 3.6 – (a) TEM of quasicrystalline particle of Al-rich Al-Mn-Be ribbons. SAED-patterns along (b) two-, (c) three- and (d) fivefold axis of the QC particle [13].

More recently in 2009 [14] the first natural occurring quasicrystal was identified in the Khatyrka meteorite with further investigations on the same meteorite leading to other two new discoveries [2,3], showing that under certain – extreme pressure and heat – conditions quasicrystals do occur naturally.

In 2021 [15] analysis of the "red" trinitite from the Trinity atomic bomb test site (Alamogordo/NM), which was formed from the fusion of the test tower and data recording equipment materials together with the soil of the explosion site, showed it to be the first anthropogenic quasicrystal, although created by chance. The icosahedral $Si_{61}Cu_{30}Ca_7Fe_2$ quasicrystal formed after the detonation is also unique, as it has not been synthesized in a laboratory, nor there is any known quasicrystal with Si, Cu, and Ca in its composition, a good example that much remains to be explored regarding quasicrystals.

3.2.2. Structure

Quasicrystals are multicomponent intermetallic compounds, which are simultaneously ordered and non-periodic, therefore lacking translational symmetry. To date only quasicrystals with 5-, 8-, 10-, 12- and 18-fold were reported in the literature [16–21]. Currently more than 20 decagonal and more than 50 icosahedral stable quasicrystals are known. The few octagonal and dodecagonal quasicrystals identified are metastable, and 18-fold symmetry only occurs under special conditions [16–18].
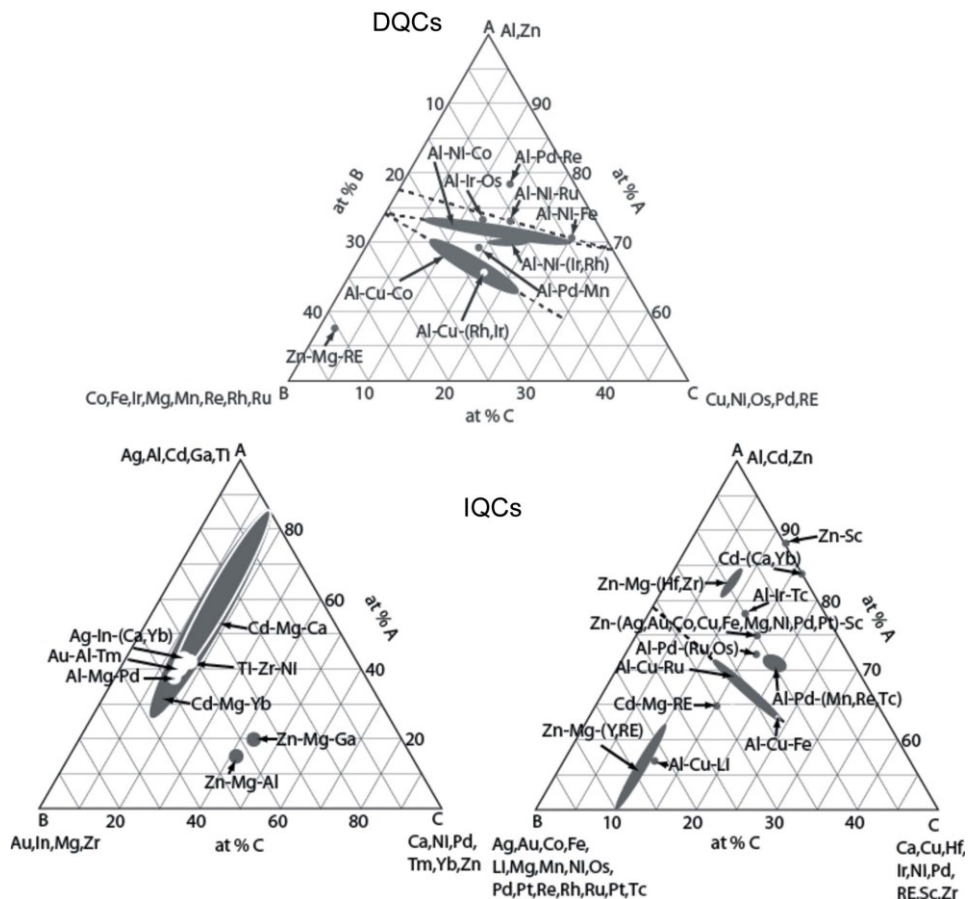
Figure 3.7 – Distribution of the known quasicrystal alloys, dodecahedral (top) and icosahedral (bottom) *[19]*.

The understanding of the quasicrystalline structure can be done from a dimensional increase perspective, meaning, from 1D up to 3D structures.

A one-dimensional crystal starting with a seed "LS", due to its periodic nature would grow by replicating its seed in each interaction. Conversely in a 2D quasicrystal, staring with a

decorated Penrose tilling forming a Ammann quasilattice as in Figure 3.8, the position of the Nth line is given according to

$$x_N = N + \alpha + \frac{1}{\tau} \left\lfloor \frac{N}{\tau} + \beta \right\rfloor,\qquad\qquad 3.5$$

where τ is the golden ratio; α and β are arbitrary real numbers and where $\lfloor\ \ \rfloor$'s represents the greatest integer function. The Eq. 3.5 which gives the position of any given grid from the origin [8].
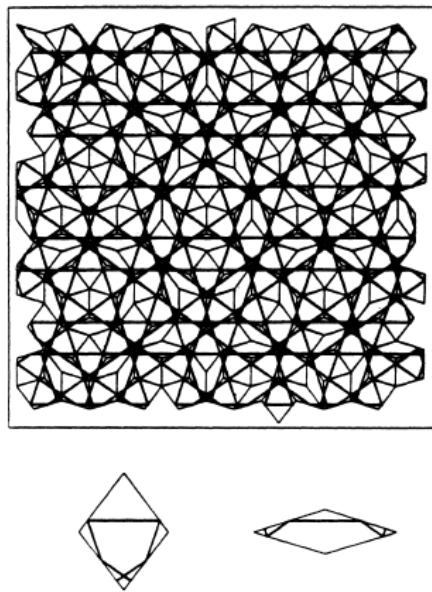
Figure 3.8 – Decorated Penrose tilling and decorated tiles as per Ammann quasilattice [8].

The 1D quasicrystal that is generated by Eq. 3.5 consists of a Fibonacci chain, generated with short segments, S, and large ones, L, which obey the "substitution" operation, L→LS and S→L, and therefore the crystal and quasicrystal structures produced are as in Table 3.I.

Table 3.I – Crystal and quasicrystal growth sequencies.

Interaction	Crystal	Quasicrystal
t_0	LS	LS
t_1	LS**LS**	LSL
t_2	LSLS**LS**	LS**LL**S
t_3	LSLSLS**LS**	LSLLSLSL
t_4	LSLSLSLS**LS**	LSLLSLSL**LSLLS**

It should be noted that if τ is an irrational number the sequence has no repetition distance. This allows us to produce a non-periodic long-range arrangement, with the ratio $L/S = \tau$, the golden ratio. The quasiperiodic translational order is extended from one dimension to two or three dimensions by adding a new element, orientational symmetry.

Moving to 3D quasicrystals they are described by overlapping layers or packaging clusters. In the Icosahedral QCs there are three main types of clusters: Mackay, Bergerman and Tsai, the former and the latter are shown in Figure 3.9.
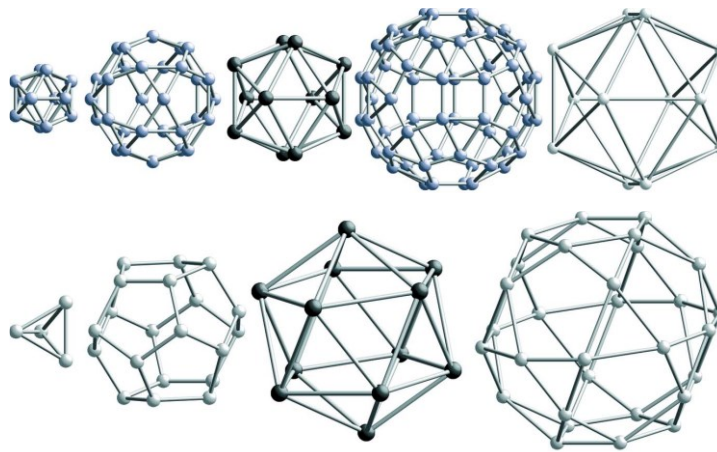
Figure 3.9 – Mackay and Tsai clusters *[17]*.

3.2.1. Fabrication Processes

Quasicrystals can be produced using different methods, including solidification of molten alloys, melt spinning, gas atomisation, mechanical alloying, electrodeposition, physical vapor deposition, gas evaporation, laser- or electron-bean superficial fusion and electron irradiation, among others. Beside these direct production methods, heat treatments can also produce quasicrystalline phases. The method used will be related to the nature of the quasicrystal to be produced, with stable quasicrystals being mostly produced by conventional equilibrium processes using casting, whereas metastable quasicrystals, which are formed by non-equilibrium phases that can only be synthesised using more advance methods, with high cooling rates [22–24].

The most common process for preparing stable quasicrystals is by melting the pure constituents into ingots, which is usually done under vacuum or inert gas atmosphere. Powder sintering is also an alternative for producing quasicrystals. These technics also allow for the growth of single crystals samples, however demanding a careful process control [22–24].

Moving to metastable quasicrystals, the production methods used are usually ones that have a high cooling rate. Among these, there is melt spinning, shown in Figure 3.10, where the liquid metal is ejected from a nozzle on the surface of spinning Cu wheel. The geometry of the wheel surface changes the aspect of the produced material, which can be ribbons or whiskers. The typical quenching rates achieved in the process are $\sim 10^4 - 10^7 °C/s$. These rates can also be increased or reduced by varying wheel speed, ambient gas, temperature of the melt or injection pressure. These changes affect both the aspect of the ribbon as well as the quasicrystalline microstructure [22–24].
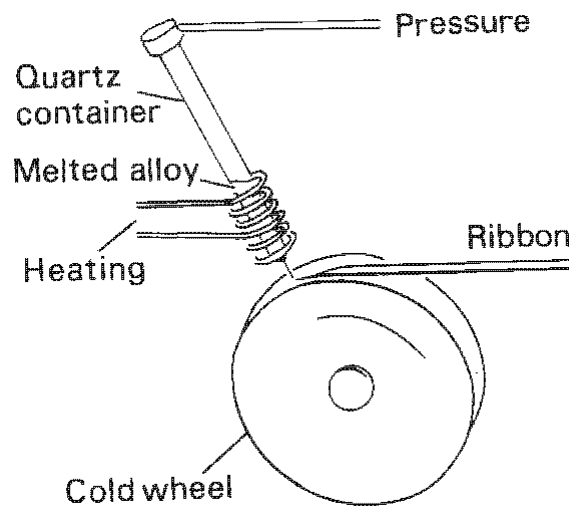
Figure 3.10 – Schematic of the melt spinning technic *[23]*.

Atomization can also provide the high cooling rates needed for synthesising metastable quasicrystals. It consists simply of the disintegration of a melt stream into droplets by using either a high-pressure jet of liquid (water or oil) or a gas (air, nitrogen, argon or helium) directed to the molten metal flow, as shown in Figure 3.11. Considering that for quasicrystals the content of oxygen, which can perturbate the equilibrium must be kept low, gas atomization is preferred as it allows for better powder cleanliness [22,25].
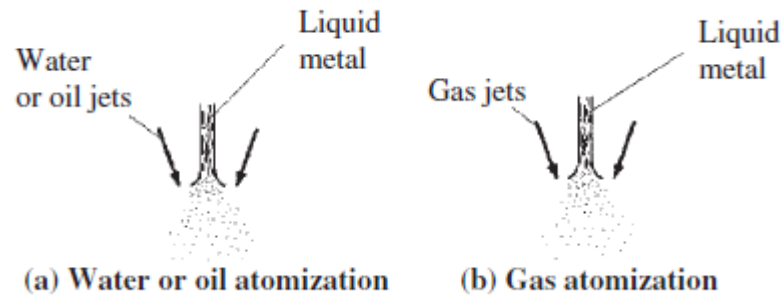
Figure 3.11 – Methods of metal-powder production by atomization: (a) water or oil atomization; (b) gas atomization *[25]*.

While water and oil atomized particles tend to exhibit an irregular shape with pronounced surface unevenness and are also prone to oxidation. On the other hand, gas atomized particles display a spherical shape and smother surface. Usually gas atomized particles tend to be less affected by oxidation unless reactive elements are present in the base melt. A model of the pressure-swirl gas atomization process is shown in Figure 3.12, displaying the transition of the melt stream towards a film, its detachment into a torus, instability of the torus, followed by breakage of the torus into the droplets [25].
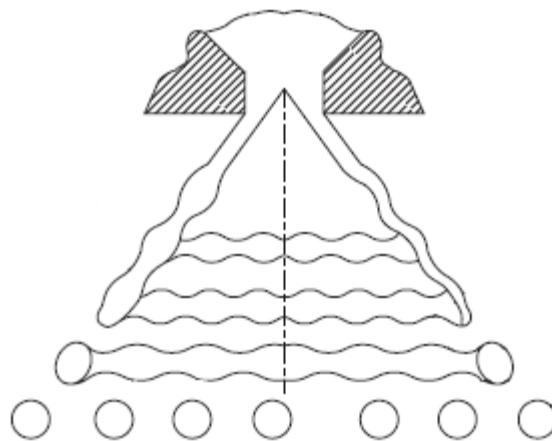
Figure 3.12 – Schematics of a pressure-swirl atomization process. Adapted from *[25]*.

For industrial production of quasicrystals, gas atomization is preferred as it allows for large batches of powder to be produced, still being much less than the amount produced through water atomization [22,25].

3.2.2. Properties

As complied by Dubois *et al.* [26–29], Laplanche *et al.* [30,31] and Fleury *et al.* [32] in a series of papers, the quasicrystals display a fair number of interesting properties, some of which are in class with those of their crystalline counterparts, which are briefly commented in the following topics.

3.2.2.1.   Mechanical properties

Usually Al-based complex metallic alloys (CMA), which are intermetallic compounds with large unit cells frequently displaying icosahedral point group symmetry (quasicrystals and quasicrystalline approximants are within this classification), are deemed too hard and brittle in their bulk form to be used in many applications. However, the hardness exhibited allows for the use of quasicrystals as tribological coatings as reported by some authors [32–38], with Sales *et al.* having demonstrated that for the Al-Cu-Fe QC the presence of the β-phase can improves the wear resistance, as shown in Figure 3.13, whereas the pure icosahedral coating has better cold welding resistance superior to that of Mo S_2 and TiC .Nevertheless, its broader application and research is limited due to the lack of adherence of the Al-based CMA and the available substrates as well as their inherent brittleness which restricts their use [28].
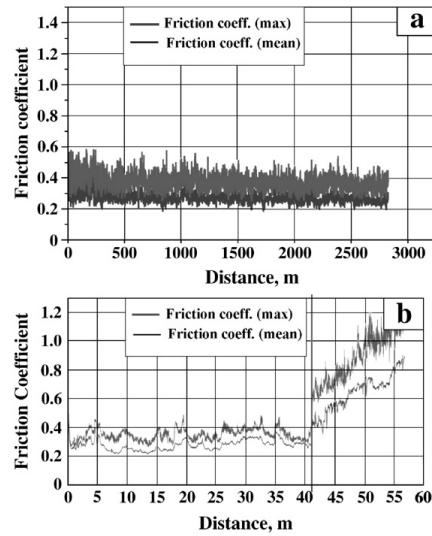
Figure 3.13 – Coefficient of friction measured between high carbon Cr-steel (AISI 52100) ball of diameter 6 mm and a flat surfaces of coatings (a) $Al_{58.5}Cu_{26}Fe_{15.5}$ (dual phase i+ψ) and (b) $Al_{60.5}Cu_{26.8}Fe_{12.7}$ (i) *[35]*.

3.2.2.2.   Thermal and electric properties

Dubois [28] also points out that complex metallic alloys (CMA), have a lower thermal conductivity than that of Al-fcc and that of alumina and silicon, it also highlights that with a low thermal conductivity the alloys can be used as a thermal barrier coating in turbines, with a similar a thermal expansion rate of the substrate. It must be pointed that CMA are not applicable in all kinds of turbines as its operating temperature may present itself as a limiting parameter.
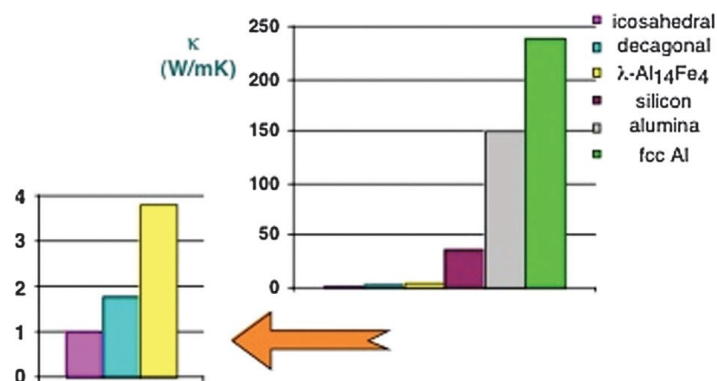
Figure 3.14 – Thermal conductivity of different materials and CMAs at room temperature *[28]*.

3.2.2.3.   Catalytic properties

Among the properties that quasicrystals exhibit the one that also draws attention is its catalytic performance [4,39–49]. It should be noted that most authors only investigated the steam reforming of methanol aided by the presence of quasicrystalline particles, with fewer authors evaluating different types of reactions with quasicrystalline catalysts, as Ngoc *et al.* [48] – butanal and ethylamine, and Mishra *et al.* – Methylene Blue [4].

Tsai and Yoshimura in 2001 [42], evaluated the effect of using $Al_{63}Cu_{25}Fe_{12}$ powder, as catalyst for steam reforming of methanol (SRM) comparing its efficiency to commercially available Cu-based catalysts. The powder ($\sim 9\mu m$) was leached using a 20wt.% NaOH aqueous solution for 2h or 12h. A solution of 1wt.% HCl was also used to leach the powder, however the only information available is that a leaching time of 2h was used, based on the results presented. While the NaOH selectively removes the Al from powder, the HCl solution removes both Al and Fe. The presence of Fe prevents Cu diffusion growth due to a sintering effect, leading to smaller particles in the NaOH leached powder and higher catalytic activity, given to the presence of Cu particles (size $\sim 15nm$) in the quasicrystal surface. The catalytic activity of the leached quasicrystal was comparable to the commercially available Cu catalysts. However, the quasicrystal brittle nature allows crushing to increase its surface area, together with tailored leaching changing its surface characteristics, better performance can eventually be achieved.

Yoshimura and Tsai in 2002 [39] went further investigating the catalytic activity of other transition metals (TM) in the stable $Al_{63}Cu_{25}TM_{12}$ quasicrystal, TM: Fe, Ru, Os, as well as other Al-Cu-Fe alloys with Ga and Co, in a steam reforming of methanol (SRM) reaction. All the formulations were leached with 20wt.% NaOH aqueous solution for 12h. Among the evaluated mixtures the one that presented the highest catalyst activity was $Al_{70}Cu_{20}Fe_{10}$, which is not a quasicrystalline alloy. However, this alloy also exhibited high temperature degradation due to its higher aluminium content, leading to the sintering of the Cu particles in the alloy reducing the H_2 production at 580k, as in Figure 3.15. This problem was not observed in the quasicrystalline alloy – $Al_{63}Cu_{25}Fe_{12}$, which shows higher catalytic activity per area. The same conclusion of Tsai and Yoshimura (2001) is presented in this work, with leached $Al_{63}Cu_{25}Fe_{12}$ displaying better catalytic activity.
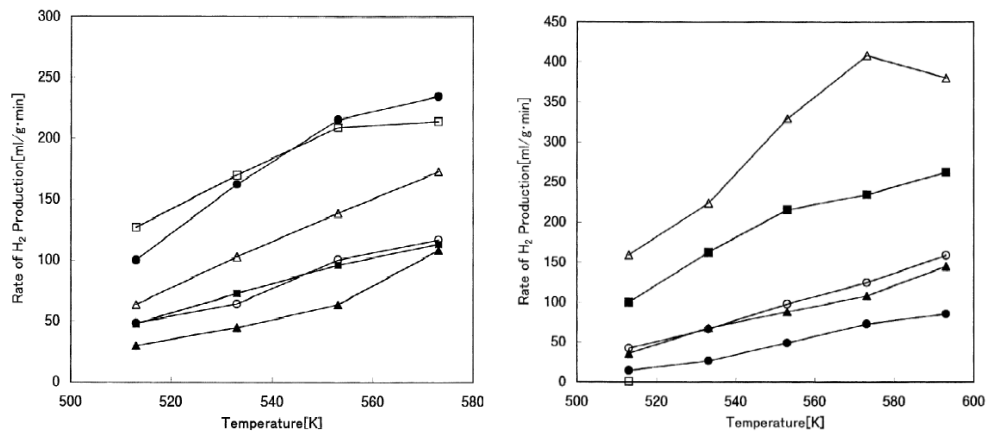
Figure 3.15 – Steam reforming of methanol, rate of H_2 production vs temperature for different QC alloys – Left: $Al_{63}Cu_{25}Fe_{12}$ (solid circles), $Al_{63}Cu_{25}Ru_{12}$ (solid triangles), $Al_{63}Cu_{25}Os_{12}$ (solid squares), $Al_{58}Cu_{25}Fe_{12}Ga_5$ (open circles), $Al_{63}Cu_{25}Fe_8Co_4$ (open triangles), Cu-based commercial catalyst (open squares); Right: $Al_{55}Cu_{30}Fe_{15}$ (solid circles), $Al_{60}Cu_{28}Fe_{12}$ (solid triangles), $Al_{63}Cu_{25}Fe_{12}$ (solid squares), $Al_{66}Cu_{22}Fe_{12}$ (open circles), $Al_{70}Cu_{20}Fe_{10}$ (open triangles) [39].

In 2004 Kameoka *et al.* [41], evaluated different Al-Cu-Fe alloy compositions either as a quasicrystal or as crystalline beta and theta phases, with a particle size <150μm, for steam reforming of methanol (SRM). Complementary to the previous works by Tsai [42] and Yoshimura [39], which used NaOH for leaching the atomized powders, Kameoka also leached with Na_2CO_3, both solutions at 5wt.%. The overall catalytic activity of the Na_2CO_3 leached powder was found to be superior to that of the NaOH counterparts, however with higher area reduction after the SRM reaction, as shown in Figure 3.16.
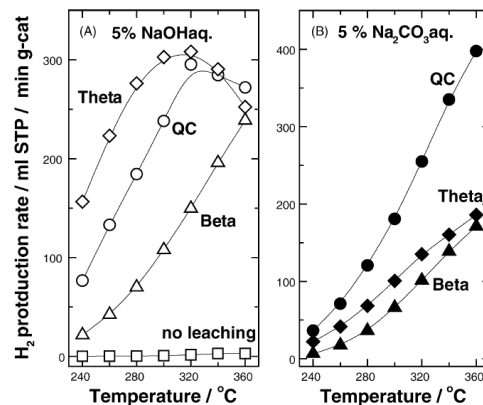
Figure 3.16 – Steam reforming of methanol for different leaching solutions, rate of H_2 production vs temperature for different QC alloys [41].

Tanabe *et al.* [43], also investigated the Al-Cu-Fe quasicrystal for SRM, focusing both on the Na_2CO_3 leaching temperature (273, 298, 323K) and milling process (dry and wet) and its effect on the surface area of the pre-reaction powder, as in Table 3.II. There was significant improvement of the surface area of the quasicrystal powder by increasing the temperature as well as by wet milling the powder. Moreover, the temperature increase leads to higher Cu surface area, which was already established as responsible for the catalytic activity of the quasicrystal, this coupled with the wet milling further increases the Cu surface area. As to the powder particle size it is only informed that it is below 150μm, for both dry and wet milling.

Table 3.II – Properties of the leached Al-Cu-Fe catalyst *[43]*.

Catalyst	ICP[a]	S_{BET}	S_{Cu}[b]	Dispersion	H_2 production rate[c]	TOF[c]
	(Al%)	(m^2 g_{cat}^{-1})	(m_{Cu}^2 g_{cat}^{-1})	(%)	(ml min^{-1} g_{cat}^{-1})	(10^{-1} s^{-1})
Before leaching[d]	–	0.6	–	–	–	–
273 K-leaching[d]	5.7	10	4.2	32.9	48	3.7
298 K-leaching[d]	13.1	32	9.5	25.6	173	5.8
323 K-leaching[d]	13.8	57	15.2	25.3	262	5.4
323 K-leaching[e]	–	89	45.2	44.2	677	4.8
Raney Cu[f]		32	30.0	5.8	181	1.9

[a] Amount of extracted Al (%) from the QC powders by the dry milling and the leaching treatment.

[b] 1.41×10^{19} Cu atoms per m^2.

[c] Reaction temperature at 573K.

[d] The QC powder was prepared by the dry milling process.

[e] The QC powder was prepared by the wet milling process.

[f] Commercial Cu catalyst (Kawaken fine Chemical Co.)

Lowe *et al.* [45] more recently explored how the leaching process affects the surface and microstructure of a single grained i-$Al_{63}Cu_{24}Fe_{13}$ quasicrystal. A solution with 40wt.% of NaOH, during 1, 2, 4, 6, and 8h, was used for leaching the sample´s surface. The previously reported selective removal of Al from the surface was also verified by the authors. Additionally, it was observed the formation of a capping layer of Cu and Fe oxides, with longer leaching times favouring the formation of Fe_2O_3 on the surface in detriment to elemental Fe and Cu. The leaching affects only the surface of the material, leaving the quasicrystal structure below unchanged.

The surface after leaching is porous with the presence of nanoparticles, with size ranging from 5-20nm. As to the porous structure formed, dodecahedral cavities showing a 5-fold symmetry, explained have origin in the surface being preferably leached along the 5-fold planes, as shown in Figure 3.17. Selected area electron diffraction (SAED) taken from the particles also showed the formation of nanoparticles of Cu, Fe, Cu_2O and Fe_2O_3. It also proposes that an interface is formed between nanosized particles observed in the leached area and the

underlying quasicrystal, which provide greater stability to the nanoparticles during catalytic reactions.
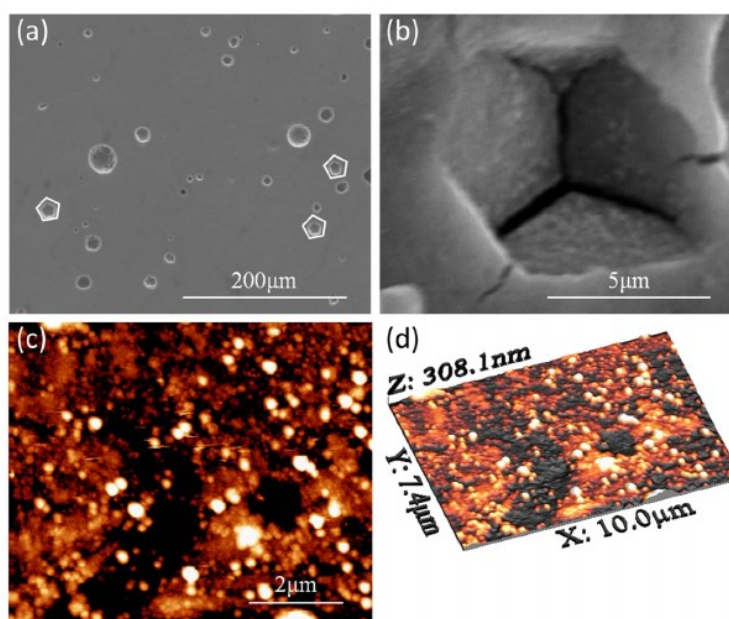
Figure 3.17 – (a) SEM image of the fivefold i-Al-Cu-Fe surface after leaching at 8 h showing 5-fold cavities across the surface (30 kV beam energy). (b) Dodecahedral cavity observed on the surface after leaching at 8 h (30 kV beam energy). (c) and (d) AFM images of precipitate nanoparticles on the surface visualized in both 2D and 3D (leaching time 8 h). AFM images were obtained in ambient conditions, not in UHV *[45]*.

Pandey *et al.* [50] evaluated a different reaction using $Al_{65}Cu_{20}Fe_{15}$ as a catalyst. Instead of SRM reaction, this time the de/hydrogenation of MgH_2 was investigated, given its potential for hydrogen storage. The usage of QC as a catalyst shows good viability, considering the cycle degradation, with a slight reduction over 51 cycles. However, there is unfortunately, no comparison with commercial catalysts. As to the catalysis mechanism a tentative atomic cluster of the bulk and milled QC was presented, showing that the leaching does remove most of the Al from the surface, leaving the Cu and Fe atoms matrix on the surface, as in Figure 3.18.
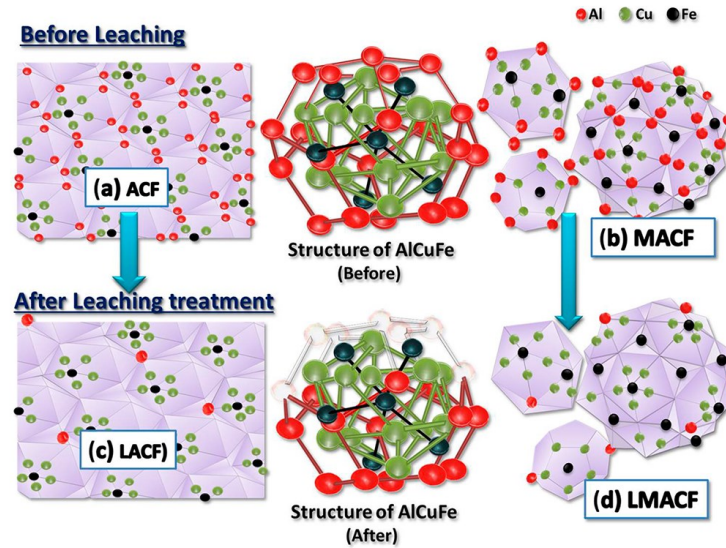
Figure 3.18 – Atomic cluster model and leaching effect on QC surface, with selective Al removal. (a) raw Al-Cu-Fe – ACF; (b) milled Al-Cu-Fe – MACF; (c) leached Al-Cu-Fe – LACF; and (d) leached and milled Al-Cu-Fe – LMACF *[50]*.

Mishra *et al.* [4] evaluated the degradation time of a solution of 0,10ml (0,1mM) Methylene Blue (MB) by the addition of 0.01g of leached $Al_{63}Cu_{25}Fe_{12}$ quasicrystals, demonstrating that the QC are able to degrade the MB, Figure 3.19, the degradation rate obtained reported was of ~0.017min^{-1}, which according to the authors lies between those values observed for pure TiO_2, $TiFe_{10}$, $TiFe_{15}$ and $TiFe_{20}$ (as catalysts), respectively of 0.0134, 0.0096, 0.0081 and 0.0064, and for the values of TiFe, $TiFe_2$, $TiFe_5$, $TiFe_7$. 0.0175, 0.0233, 0.028, 0.042, respectively.
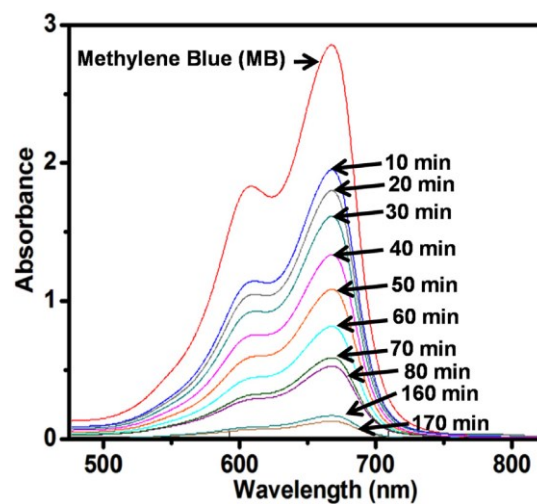
Figure 3.19 – Methylene Blue degradation time [4].

3.3. The Al–Cu–Fe System

The AlCuFe system was first investigated by Bradley and Goldshmidt in 1939, when they reported an unknown ψ-phase, for which the ideal formula proposed was Al_6Cu_2Fe, and the average composition in the single phase region $Al_{65}Cu_{22.5}Fe_{12.5}$ [22].

Following the discovery of quasicrystals by Shechtman in 1984 [1], many researchers started to look for alloy systems that could lead to the formation of stable quasicrystals [51]. Tsai *et al.* reported in 1987 the synthesis of a stable Al-Cu-Fe icosahedral quasicrystal prepared using rapid and conventional solidification, which could be followed by annealing, in a composition range from 16 – 24 at% Cu and 11 – 17 at% Fe, with the remaining being Al [52]. The produced alloy was $Al_{65}Cu_{20}Fe_{15}$, which according to the differential thermal analysis (DTA) shows only one endothermic peak at 1135K, the alloy melting temperature, and no other peak was observed indicating that there were no other phase transitions, showing that the quasicrystalline alloy consisted of a single phase.

Faudot *et al.* in 1991 [53] went to further characterize the phase transformations involved in the formation of the i-phase in the Al – Cu – Fe system, by fabricating alloys with varying Cu-Al compositions, summarizing them on a ternary diagram and on a pseudo-binary diagram, as Figure 3.20.
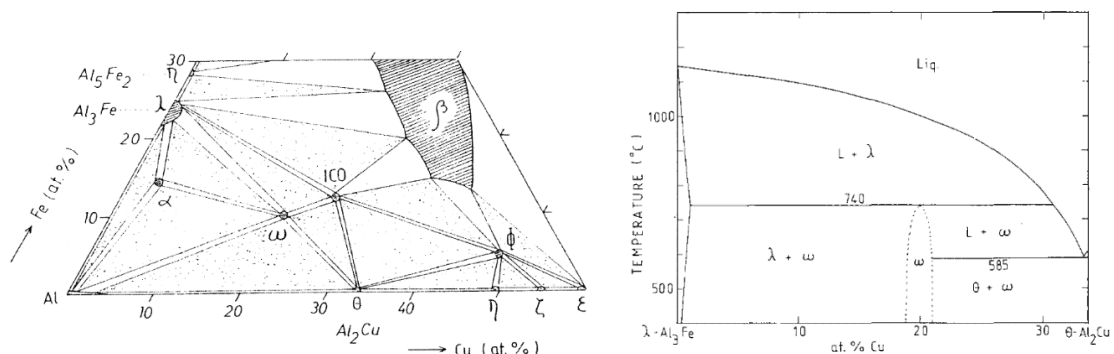
Figure 3.20 – Ternary diagram and pseudo-binary diagram for the Al-Cu-Fe system *[53]*.

In the composition ranges between $Cu_{24}Fe_{12}$ and $Cu_{25.5}Fe_{12.5}$ the as-quenched samples presented, beside the icosahedral QC, there is also the presence of β-phase which disappear after annealing. While lowering the Cu-Fe content induces the presence of the icosahedral phase together with Al_2Cu, both of which after annealing turn in the ω-phase, an increase in the Cu-Fe content leads to the formation of icosahedral phase together with β-phase, with the later

becoming dominant after annealing, and in the $Cu_{28}Fe_{14}$ being the only phase identified in both conditions – as-quenched and annealed.

Fadout also proposes the reactions that took place during DTA analysis of the $Al_{63}Cu_{25}Fe_{12}$ following various heat treatments, which are as follows:

  i. $820^{o}C$ – $860^{o}C$ the reaction from i → liquid + i occurs.
  ii.   At $870^{o}C$ the i-phase reacts peritectically with liquid forming phases β and λ.
  iii. Above $900^{o}C$, increase in the liquid phase and formation of the high temperature phase Al_3Fe.
  iv.   Above $1000^{o}C$ the alloy is totally melted.

With the previous DTA analysis it was also proposed a simplified vertical section of the phase diagram, which displays the phases that exist in equilibrium in the different temperatures evaluated. Albeit not a pseudo-binary diagram, it allows to understand some effects related to the annealing conditions, Figure 3.21.
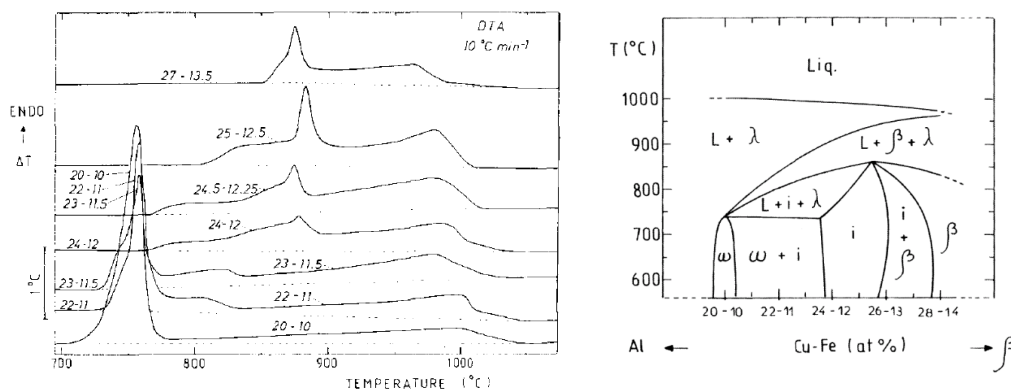
Figure 3.21 – DTA curves of various Al-Cu-Fe compositions and simplified vertical section derived from the DTA curves *[53]*.

Huttunen-Saarivirta [22] points out that the icosahedral phase is stable at high temperatures over a range of compositions, as Tsai and Fadout had already demonstrated. It also highlights that the fraction of the quasicrystalline phase is strongly dependent on the Fe concentration in the alloy. The alloy composition and cooling rates also plays a major role as to each phase will be predominant, with higher cooling rates leading to the direct formation of que icosahedral quasicrystalline phase, however, as demonstrated previously subsequent

annealing can lead to an increase in the quasicrystalline phase fraction if the material was slow cooled from the liquid.

3.4. Catalysis

The history of "catalysis" was first recognized by Berzelius in 1835 [54]. Catalysis is a kinetic rather than a thermodynamic phenomenon, as it is based on lowering activation barriers and speeding up reactions and not on changing equilibria. It cannot alter the equilibrium concentrations of reactants and products in each reaction. Generally, the rate constant, k, of a reaction depends on the activation energy:

$$k = ve^{-E_{act}/RT}, \qquad\qquad 3.6$$

where v is the pre-exponential factor, R is the gas constant, and T is the temperature. One can quickly notice that a decrease in the activation energy increases the reaction speed, as shown in Figure 3.22, where an intermediate lower activation energy surface reaction occurs speeding up the global reaction [55].
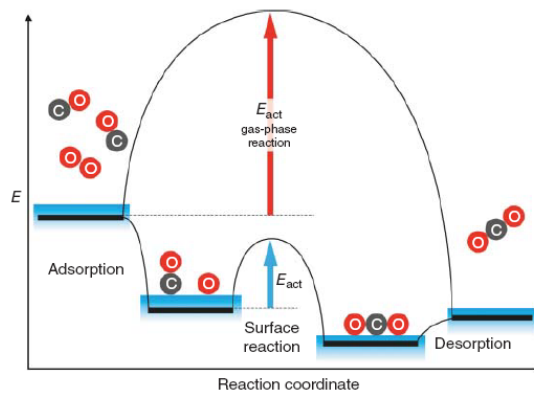
Figure 3.22 – Potential energy scheme of a heterogenous catalysis of CO oxidation *[55]*.

The catalytic phenomenon can be divided in three areas, as follows:

- Homogenous catalysis,
- Heterogenous catalysis, and
- Biocatalysis.

Considering the application of quasicrystals as catalysts, which are in a different state of the reactants, the following discussion will be focused on heterogenous catalysis.

The application of heterogenous catalysis, on which 80–90% of all chemical process rely on, are mainly used in the manufacture of chemicals, fuel production, and environment protection [55].

On fuel production, while on the beginning most fuel was produced through distillation, increase in demand led to the need of speeding up reactions and increasing production. To do so, new reaction routes were discovered with the use of heterogenous catalysts, used on catalytic reforming (linear to aromatics), catalytic cracking (heavy hydrocarbons into lighter ones), hydrotreating (S, N and O removal), and the conversion of natural gas into liquid fuels [55].

As to chemicals the production of ammonia, developed in the 20th century by Haber and Bosch, which allowed the mass production of fertilizers, is a key example, as it allowed for millions of people to be fed [55].

On the matter of environmental protection, the usage of catalyst in cars was a major player in reducing the amount of NO_x and SO_x emissions [55]. It must also be noted that not only air is subject to contamination, but water can also be affected by anthropogenic contaminants such as dyes from textile industry[56,57].

All these catalytic reactions can be summarized in the same cycle, of five steps, as follows, shown in Figure 3.23 [55]:

     I.   Transport of the reactant to the active site

    II.   Adsorption of the reactant

    III.   Surface reaction between the adsorbed intermediates and product(s)

    IV.   Desorption of the product(s)

    V.   Transport of the product(s) from the active site
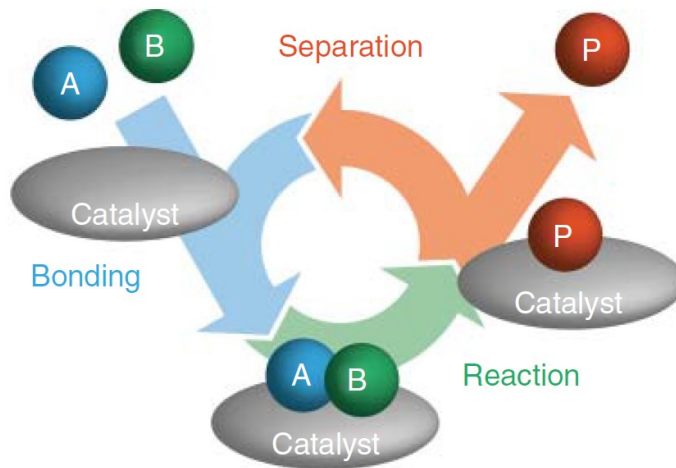
Figure 3.23 – Catalysis cycle *[55]*.

The characterization of a catalyst is made by its surface area and porosity [58], as well as by the number of active sites and state at reaction condition. Pore volume can be measured using the BET adsorption isotherm as follows

$$\frac{P}{V_{ads}(P_s - P)} = \frac{1}{CV_m} + \frac{C-1}{CV_m}\frac{P}{P_s},$$ 3.7

V_{ads} is the volume of gas adsorbed and V_m is the volume per molecule, P_s is the saturation pressure at the condensation temperature of the gas, and C is equal to K_{ads}^0.

While being affected by the proposed catalyst porosity, catalysis is also modelled after Langmuir Adsorption Isotherms. They relate the concentration of the adsorbed species to the partial pressure of the adsorbing molecule, as in Equation. 3.8,

$$\theta = \frac{K_{eq}\dfrac{P}{P_0}}{1 + K_{eq}\dfrac{P}{P_0}},$$ 3.8

where θ is the fraction of surface sites occupied by the adsorbing gas, P is the gas pressure, P_0 is the pressure of gas at standard pressure and temperature conditions, and K_{eq} is the equilibrium constant of adsorption defined as the ratio of the rate constant of adsorption k_{ads}, and the rate constant of desorption k_{des}.

It should be noted that there is a direct relation for catalysis with the number of active sites for adsorption, which can be increased by a larger surface area, or when not possible by

increasing the catalyst concentration in a process, both of which increase the rate constant and decreases the degradation time.

To some authors the degradation of dyes in heterogenous (photo)catalysis flows a pseudo-first order decay kinetics, modelled after Langmuir-Hinshelwood equation:

$$ln\frac{C_t}{C_0} = k_{app}t \qquad 3.9$$

where C_t is the concentration at a given time t, C_0 is the initial solution concentration, k_{app} is the apparent constant rate.

3.5. Congo Red

Congo Red (CR) belongs to the category of direct dyes, which can dye cotton 'directly' without the need of a mordant (which is a substance used to better bond the dye to the fabric improving its durability). They are classified following many parameters, such as their application characteristics, fastness and more relevant their chromophore. A chromophore is the part of a molecule that is responsible for its colour, it is also where the absorption occurs in the molecule and where there is a major change in the molecule geometry and electron density, which often consist of conjugated bonds and/or rings [59]. The more relevant chromophores are azo, stilbene, phthalocyanine, dioxazine and other smaller chemical classes such as formazan, anthraquinone, quinoline and thiazole [60]. The chromophores presence in Congo Red is of the azo type, due to the double $-N = N-$ bond, more specifically diazo given the molecule symmetry.

Congo Red was invented by Paul Bottiger in 1884 [61] by reacting bis-diazotised benzidine with two molecules of napthionic acid, as shown in Figure 3.24, which produces a red powder after drying. The dye patent was later bought by the AGFA company who mass produced and commercialized it under the name "Congo Red" [60].

The use of azo has declined over the years due to its known carcinogenic properties, which were compiled by Brown and DeVito [57] based on others research, who showed the possibility of such dyes giving origin to one of the following mechanisms:

- Azo dyes which are toxic after reduction and cleavage.
- Azo dyes with aromatic amine groups which can be metabolized.

- Azo dyes that may be activated through direct oxidation of the azo linkage.

Among the findings reported on Congo Red, after the azo reduction to its benzidine constituent, an aromatic compound, mutagenic activity was induced in the tested bacteria and mice [57].

Its use was further restricted after the approval of the German Consumer Goods Ordinance which came into effect in 1996, which banned the use of some azo dye, and as such the Congo Red has been withdrawn from use and manufacturing by many chemicals manufacturers. Additionally the wash-fastness of these dyes is only moderate, which also led to the industry preference for reactive dyes with higher wash fastness on cotton and similar textiles [60]. Its use is now limited to histology sample preparation and as an acid-base indicator.
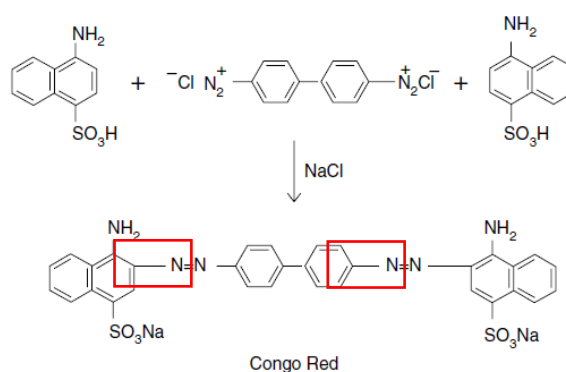
Figure 3.24 – Congo Red production reaction, the azo chromophores are highlighted in red *[60]*.

3.5.1. Congo Red Degradation

The use of dyes has been common in (photo)catalytic degradation experiments, as they allow the use of UV-Vis spectroscopy; are relatively cheap, are easy to use and to measure its degradation kinetics, although some limitations are present such as the presence of other species [62]. Another advantage of using dyes is that as either adsorption or catalysis occurs, the solution colour changes as the chromophore is removed or degraded in the process.

Several authors have studied the catalytic effects of different kinds of compounds for Congo Red degradation, some of which are compiled in Table 3.III.

Table 3.III – Effect of different catalysts for degradation of CR

Catalyst	Catalyst Concentration [mg/l]	CR Concentration [mg/l]	Photocatalysis	Reference
$Co_{1-x}Cu_xFe_2O_4$ (x = 0, 0.5)	200	10	Yes	Kirankumar[63]
$PbTiO_3$ Nanorods	250, 500, 750, 1000	7, 8.7, 17.4, 26.1, 35	Yes	Bhagwat[64]
Natrojarosite	2000	30	Yes	Dong[65]
$Fe^{3+}/(NH_4)_2S_2O_8$	2, 6, 10, 15, 20	5, 10, 15, 20	Yes	Devi[66]
Activated Hydrotalcites	666 + Cu Anode	400	Yes	Argote-Fuentes[67]
TiO2	700, 1000, 1300	50, 100, 150	Yes	Sakkas[68]
CuO Nano-rods, -sheets, - leaves	500	20	Yes	Sadollahkhani[69]
$Cu_2(2,2'-bipy)_2(pfbz)_4$	167	60	No	Han[70]
Cu_2S decorated Cu_2O nanocomposites	10000	200	both	Yue[71]

Devi using Photo Fenton like process using Fe^{3+} ions as catalyst and peroxide disulfate as oxidant proposed a degradation mechanism for Congo Red [66], while Dong used jarosite-type compounds proposed an alternative path for CR degradation [65] and Bhagwat investigated the photocatalytic properties of $PbTiO_3$ nanorods on CR [64], all these paths are exemplified in Figure 3.25.

These degradation pathways were proposed based on the results of either Gas chromatography–mass spectrometry (GC-MS) [64,66] or Electrospray ionization mass spectrometry in the negative ion mode (ESI(–)-MS) [65]. These analyses allow to measure the mass to charge ratio (m/z), and predict the possible compounds generated after a defined time. Considering the different kinds of catalysts used in the experiments, the different paths proposed by the authors is not surprising. Although it should be noted that all paths begin with the breakage of the double azo bond in CR.
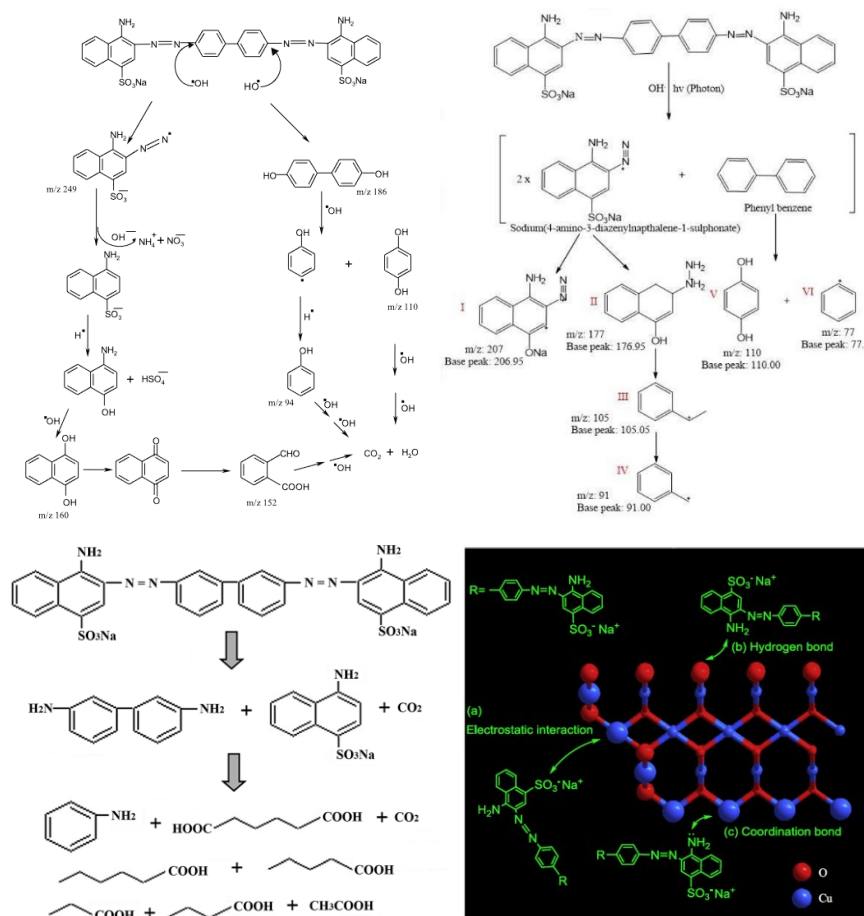
Figure 3.25 – Proposed Congo Red degradation path – Above left: using Fe^{3+} [56]; Above right: using $PbTiO_3$ nanorods [64]; Below left: using natrojarosite [65]; Below right: Using Cu_2O nanoparticles [72].

The decomposition products are different, however there seems to be an agreement between the authors that the used catalysts produce reactive oxygen species such as $^{\bullet}O_2^-$ and $OH^{\bullet}$, which are needed to accelerate the catalytic reaction which leads to the degradation of CR. The same effect is obtained when is present Cu_2O with the radical $^{\bullet}O_2^-$ being prevalent, withs effect enhanced by h^+ in the case of photocatalysis [71]. This can also be achieved or enhanced by either adding H_2O_2 or by photoactivation, when the catalyst absorbs a photon [64,69,70] altering the catalyst valence state.

4 MATERIALS AND METHODS

4.1. Powder fabrication

The sample powder of the $Al_{62.5}Cu_{25}Fe_{12.5}$ (%at.) alloy, was manufactured through gas atomization using commercially pure elements (>99%). The base metals were induction melted and poured in the atomization chamber at 1200ºC. A 4mm nozzle was used, through which the material flowed. Nitrogen was used as atomization gas, with a nominal pressure of 10bar. The solidified powder was collected and sieved in different granulometric ranges, for further experiments. In the present work, particle sizes ranging from 53 to 106 µm were used. This was conducted at the foundry lab of the Department of Materials Engineering of UFSCar (Federal University of São Carlos).

Following catalytical proof of concept tests with the powder with particle size 53 to 106 µm, it was decided to further reduce the average particle size to be below 20 µm. High energy ball milling was performed in a planetary ball mill, under argon atmosphere. The milling process was conducted for 1h for each batch, using 600 rpm of rotational velocity and ball to powder ratio of 10:1. These finer powder particles were used on the catalytic tests.

4.2. Chemical treatment

To increase the powder´s surface area and to activate its catalytic properties, the samples were preliminarily leached using a NaOH solution (10mol) during different times, 0,5h, 3h, 5.5h, and 8h, as tested elsewhere[4,39,41,43,50,73], with 5g of starting powder in each case. After each period, the powder was washed with deionized water and dried at 100 °C. In this first test, the as-atomized powder was used (due to the larger volume of material needed to perform the experiments).

After comparing the particle morphology and BET results of longer leaching times in the powder particles, as to the particle depth that was reacting and having material removed by the leaching solution, no significant difference was noted by increasing the leaching time beyond 3h, therefore for catalysis experiments conducted in the present work the leaching time was limited to 3h. The finer powder (after ball milling) was therefore leached in the NaOH solution for 3h prior to the catalytic experiments.

4.3. Microstructural characterization

4.3.1. X-Ray diffraction analysis (XRD)

X-Ray diffraction analysis was performed in the Department of Metallurgical and Materials Engineering (DEMET) of UFMG, using a Philips-PANalytical PW 1710 of the X-Ray diffraction Laboratory of DEMET-UFMG, using CuKα (λ = 1,54 Å) radiation and a measuring step of $0,06^\circ s^{-1}$.

The XRD were results used to characterize the phases formed in the atomized material and after leaching.

4.3.2. Gas Adsorption - BET

The powder prior and after leaching was submitted to an adsorption analysis to evaluate the change in its surface area and the pore size distribution, both of which play a major role in the catalytical performance of the powder. The analysis was conducted in a Quantachrome Nova 2200e, the samples were held under vacuum for 24h at 110°C. The tests were performed using N_2 (99.999% purity), approximately at -196°C. The specific area and pore size distribution was then measured.

4.3.3. Scanning Electron Microscopy (SEM)

The atomized and leached samples were analysed using SEM for morphological and microstructural characterization. The analysis was conducted in the Scanning Electron Microscopy laboratory of DEMET, using a SEM – INSPECT FEI with an attached EDS detector and a W source. The samples were prepared by mounting the powder samples into a resin, followed by conventional metallographic procedures. The samples were not chemically etched after polishing. Samples were coated with a gold film prior to the SEM analysis.

4.3.4. Transmission Electron Microscopy (TEM)

Aiming for a more detailed characterization of phase structure formed after the leaching of the powder, a sample was characterized using transmission electron microscopy. The $< 20\mu m$ milled particles after 3h leaching was prepared by UFMG's Microscopy Centre, using a small amount of powder dispersed in isopropyl alcohol and sonicated. The suspension was then

pipetted into a Ni grid and left to dry, before being used in the TEM analysis and imaging. A Ni grid was used, instead of the usual Cu grid, to prevent noise in the EDS results, as the samples also possess Cu in its composition.

The analysis was performed in UFMG's Microscopy Centre, using a TEM-TECNAI FEI Supertwin, with a LaB_6 source, operating at 200kV. The TEM has EDS and EELS systems coupled; the EDS system was used to identify the present elements whereas the EELS system was used to identify the oxidative state of the remaining Cu in the particles.

4.4. Catalytic Performance Characterization

The samples, after leaching, were tested for their catalytic activity. Congo Red was dissolved in water with a concentration of both 50 and 150mg/l and the influence of the quasicrystalline particles in the degradation of the organic molecules evaluated with a concentration of 500mg/l, in the following combinations:

- 50mg/l CR + 500mg/l Al-Cu-Fe,
- 150mg/l CR + 500mg/l Al-Cu-Fe

The total volume of the solution prepared for each one of the experiments was of 400ml, and the solution samples collected in the following intervals – 0, 10, 20, 30, 40, 50, 60, 70, 80, 90, 100, 120, 140, 160, 180, 200, 220, 240, 260, 280 and 300 minutes. After the last collection, the samples were left to further react to evaluate the effect of a longer reaction time, up to 7200 minutes.

The samples were of 10ml, which were centrifuged for 5 minutes in falcon tubes to separate any dispersed powder particle from the solution to be analysed. From the centrifuged solution a 4ml sample was taken and placed in a cuvette for UV-Vis spectroscopy analysis.

The dye concentration (organic molecules) before and after the exposure to the quasicrystalline particles was evaluated by UV-Visible spectroscopy using a Shimadzu UV-2600.

To evaluate the degradation progression a calibration curve was also made, varying the concentration of CR from 0mg/l up to 150mg/l, with measurements done in the same way as with the testing samples.

5   RESULTS AND DISCUSSION

5.1. X-Ray diffraction analysis (XRD)

Powder x-ray diffraction was conducted on both the as received powder as well as on selected leached powder, namely 0,5h, 3,0h and 8h. The obtained patterns show that longer leaching times reduced the characteristic peaks regarding the icosahedral quasicrystal present in the non-leached powder, as in Figure 5.26
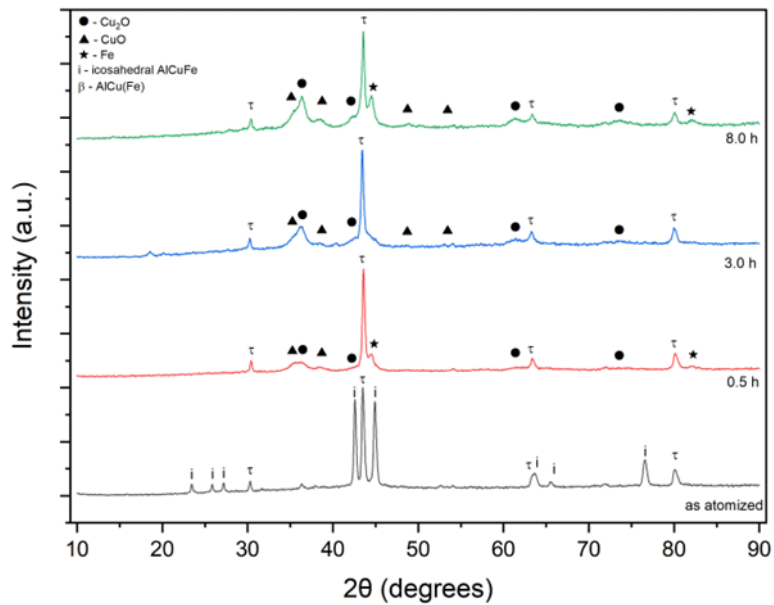
Figure 5.26 – XRD results for the powder samples.

The leaching process alters the specimens present in the powder. It is noticeable that the peaks regarding the icosahedral quasicrystalline phase are strongly reduced in all leaching times, associated to the intense removal of Al by the alkaline chemical attack as reported by Tsai *et al.*[42]. While the QC was nearly completely removed the τ-phase remained in all leached powders irrespective of attack time. In the treated powder structure new phases were identified, namely CuO and Cu_2O, as shown in the Figure 5.26. Increasing the leaching time leads also to the increase of the intensity of the peaks related to CuO and Cu_2O, as well as to the broadening of these peaks. The peak broadening is associated with smaller sized crystallite sizes, following Scherrer relation, considering the prevalence of the τ-phase in the samples the peaks changes observed are related to modification of its surface by the alkaline solution [45].

It can also be noted that for the 0.5h and 8.0h leaching times a noticeable amount of Fe was identified in the powder samples, this could be due to iron oxides degradation during leaching and

5.2. Scanning Electron Microscopy

The powder before the leaching shows a prevalent spherical shape, Figure 5.27, which is expected considering the production process used. Mounting the powder with the following polishing process allows the powder microstructural analysis, as seen in Figure 5.28, where two major phases can be observed.

It should be noted that some particles display a thicker outer layer, highlighted in Figure 5.28, known as core-shell structure, due to segregation that occur during the cooling of the atomized droplets, which can be caused by different factors, among them spinodal decomposition, surface wetting, droplet drifting, collision and coagulation, and Marangoni motion. Another possible explanation is that the quenching time was simply too high to allow for a complete phase transformation in the particle, as expected in atomization.
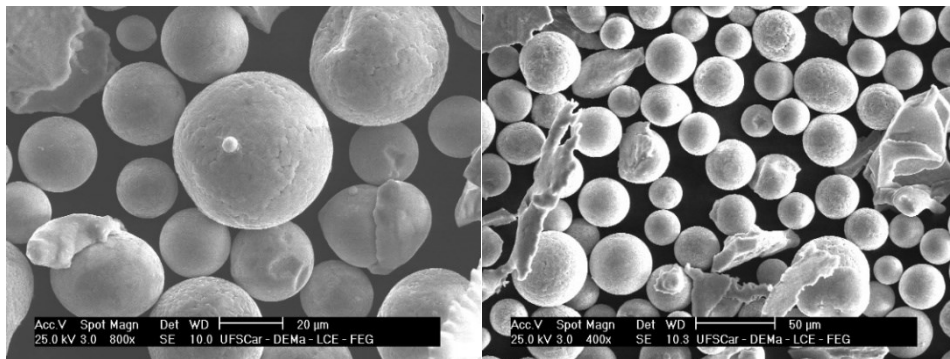

Figure 5.27 – Particle prior to leaching exterior morphology, courtesy of Witor Wolf.
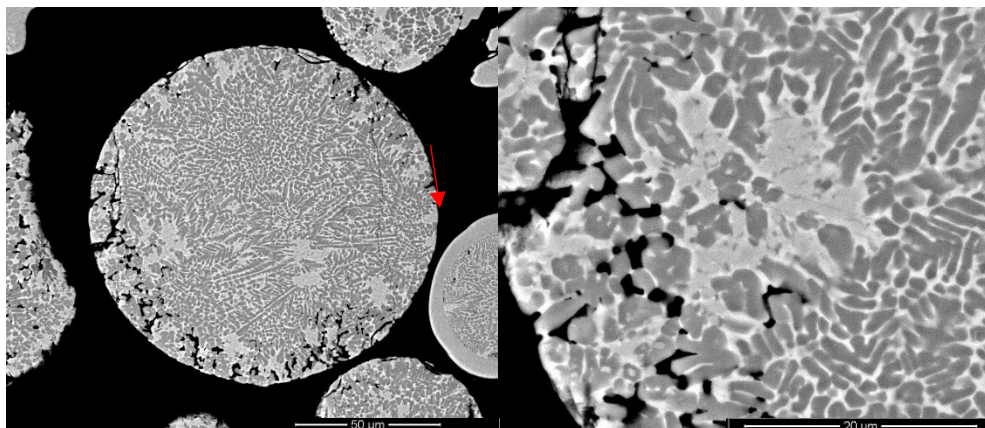

Figure 5.28 – Particle prior to leaching interior morphology, the arrow indicates the outer layer in one of the particles. The darker phase is the QC phase in the particles.

In the samples it was also possible to identify the prevalent composition of the phases that constitute the Al-Cu-Fe powder, using the EDS detector, as in Figure 5.29, where that Al, Fe and Cu are all present in the non-leached material, with Fe and Cu nearly evenly present in the sample and Al more present in the darker areas of the particle. Although the EDS resolution was not enough to show, there is Cu-rich phase in this microstructure, named τ-AlCu(Fe) that forms in a skeletal morphology, being surrounded by the QC phase (darker phase in Figure 5.29).
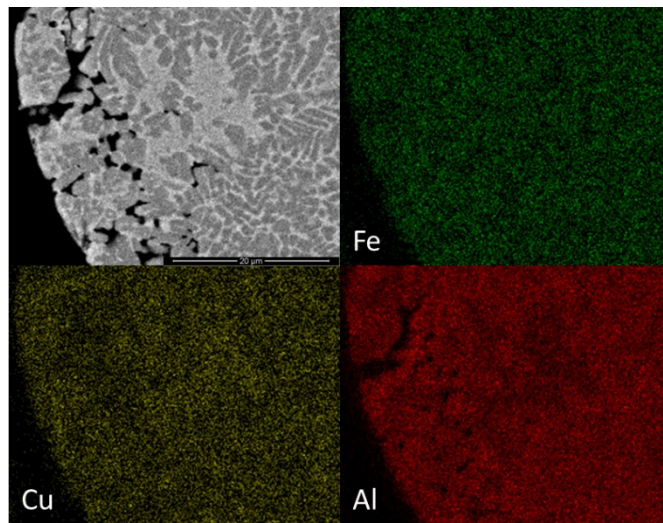
Figure 5.29 – EDS of a particle before leaching, showing its components.

After leaching the Al rich phase was partially removed, given the percolation of the NaOH solution in the particle structure leaving a skeletal structure, as in Figure 5.30. The leaching process also led to some particles being leached to a point in which they broke apart. This skeletal structure belongs to the phases poorer in Al (from the as-atomized particles) which were less affected by the leaching process. As it will be seen in the TEM analysis, most of the particles of the leached powder were Cu-rich (and sometimes Fe-rich) and with the XRD patterns, one can infer that this skeletal structure is mostly due to the presence of the τ-AlCu(Fe) phase in the as-atomized powder. The presence, in a lesser extent, of the β-AlFe(Cu) also explains some Fe-rich regions after leaching. Both τ and β phases present the same unit cell and lattice parameters. They cannot be separated in the XRD pattern. However, they have different proportions of Fe and Cu.
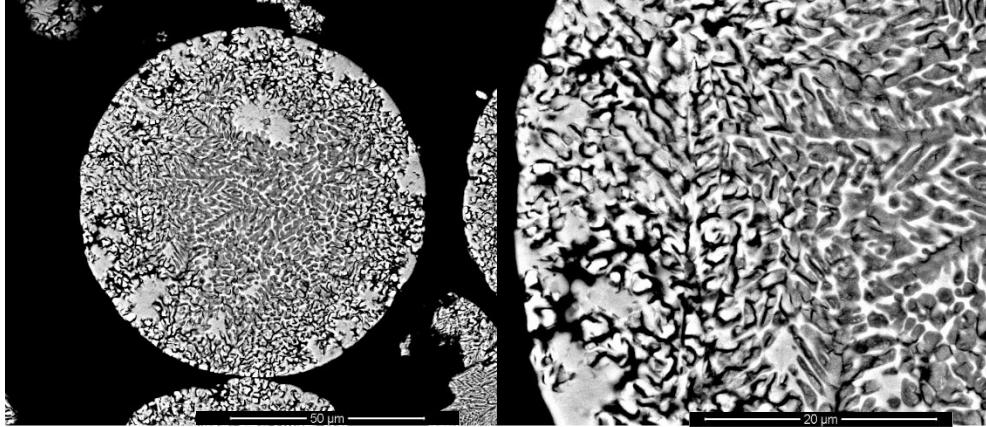
Figure 5.30 – Particle interior morphology after 0.5h of leaching

The remaining structure of the particle after the leaching is rich in Cu and Fe as in Figure 5.31, in which it can also be noted a reduction in the Al rich phase content in the direction of the particle centre.
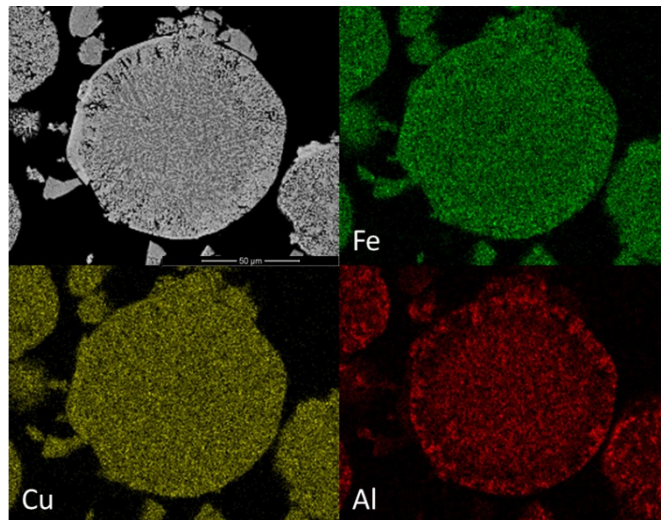
Figure 5.31 – EDS of a particle after 0.5h of leaching, showing its components.

Increasing the leaching time, from 0,5h to 3h, as expected, also increases the amount of Al rich phase removed from the particles. The longer leaching times expands the freely available area of Cu rich phase in the particles, hence it can be said that the Al rich phase is used as a scaffold around which the Cu rich phase grows and upon removal exposes it.
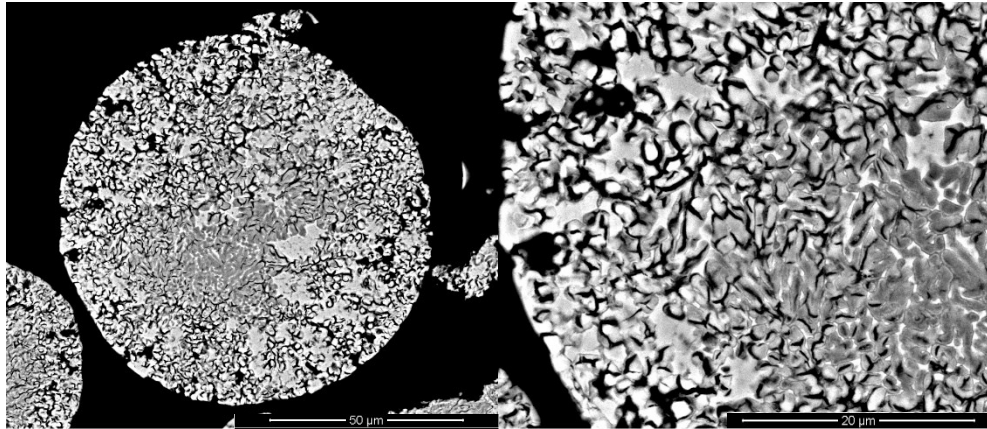
Figure 5.32 – Particle interior morphology after 3h of leaching

In the analysed particle the leaching process left clusters of the Al rich phase (QC) because they are embedded deep in the particle to be fully removed by the leaching agent, which was either because of poor percolation in the particle interior or due to insufficient time for the leaching solution to reach and react with these parts of the particles.
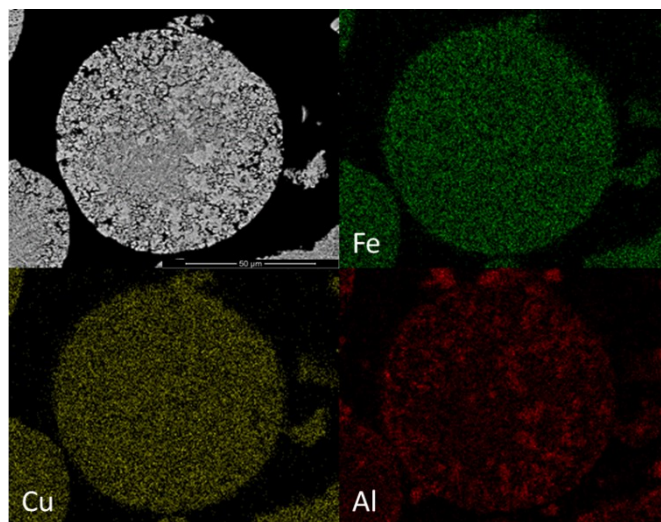
Figure 5.33 – EDS of a particle after 3.0h of leaching, showing its components.

Longer leaching times as 5.5h, and 8h, lead to the removal of more Al rich phase, as well as to increase the number of fragmented particles in the powder sample, as can be seen in Figure 5.34 and Figure 5.35, in which more fragments are around the particles and after the 8h leaching time they even form clusters.
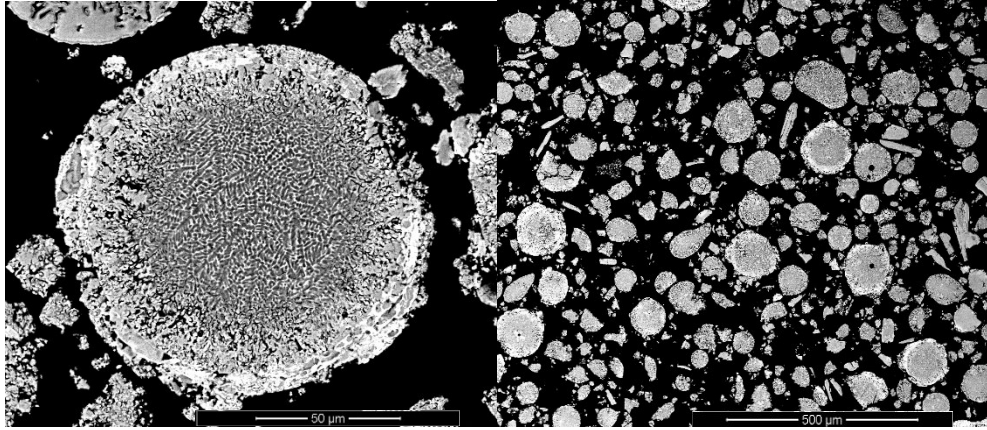
Figure 5.34 – Particle interior morphology after 5.5h of leaching
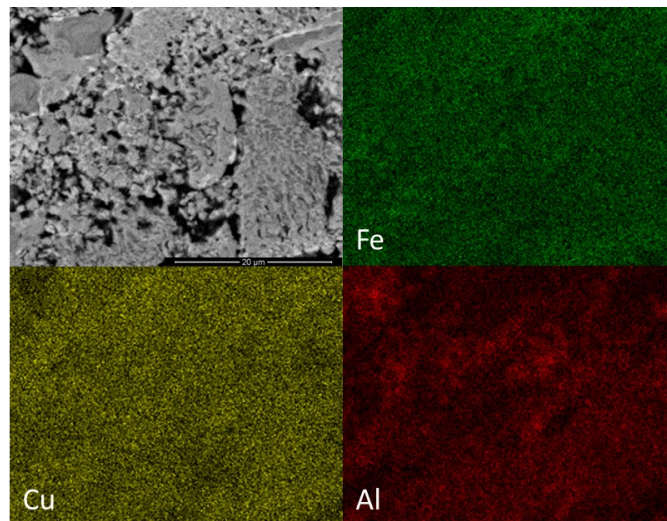
Figure 5.35 – EDS of a particle after 5.5h of leaching, showing its components.

The 8h leach period, lead to the removal of more Al rich phase, and to most particles losing their structural integrity, as most of the particles being no longer rounded scaffolds, but an aggregate of fragments originated in this breakage, as in Figure 5.36 and Figure 5.37.
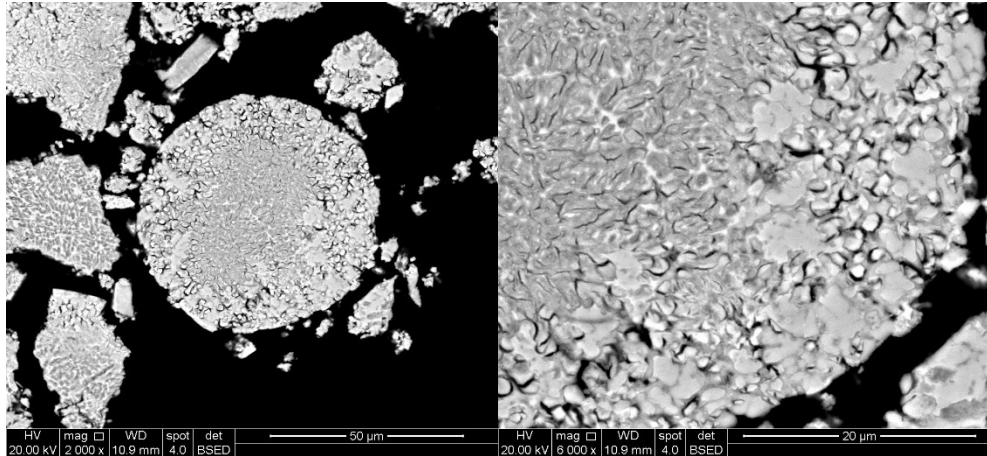
Figure 5.36 – Particle interior morphology after 8h of leaching
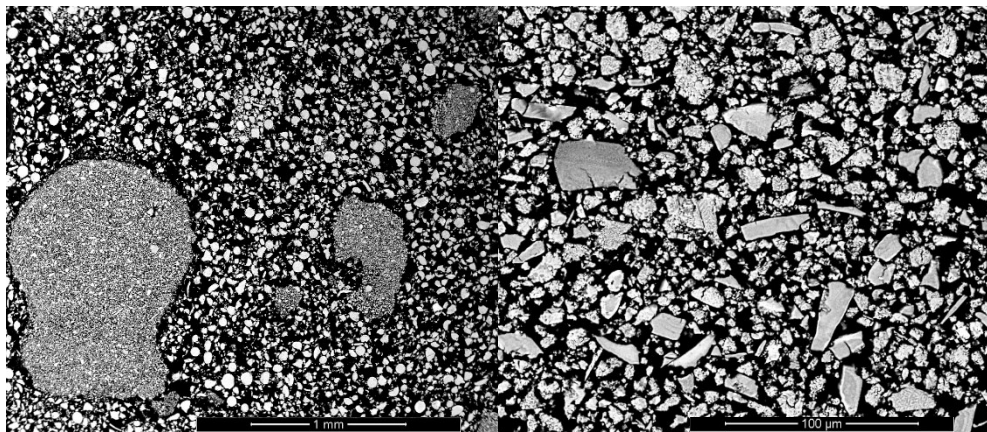
Figure 5.37 – Particles fragments after 8h of leaching and zoom into one of the fragment clusters.

The powder used in the catalysis experiments was ball milled to further reduce its size, the aspect of the milled powder can be seen in Figure 5.38. The leached powder, similarly, to what happened in the other samples also shows an increase of the smaller sized particles due to structural strength lost by the removal of the QC phase.
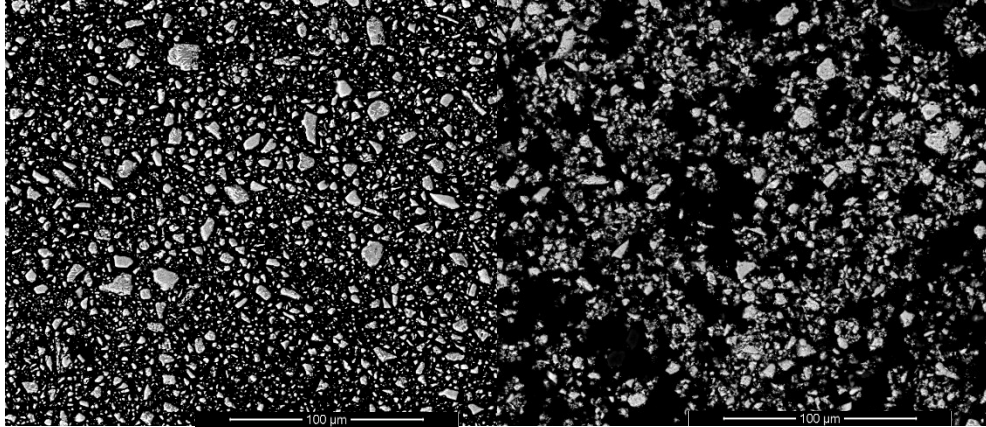
Figure 5.38 – Right: Particles of the powder after milling. Left: milled and 3.0h leached powder.

5.3. Gas Adsorption - BET

The BET analysis was performed on all the leached samples as well as on the powder before leaching. The isotherms in Figure 5.39, show the adsorption and desorption of the powder samples.

The isotherms produced in the analysis are of Type IV, considering IUPAC classification, with the presence of a hysteresis loop H4. It can be noted that at higher relative pressures (> 0.8) the 0.5h powder increases its adsorbed volume more than the other leached samples, a possible explanation for this effect is its average pore size after an insufficient leaching time to remove enough material from the particles creating smaller sized pores.
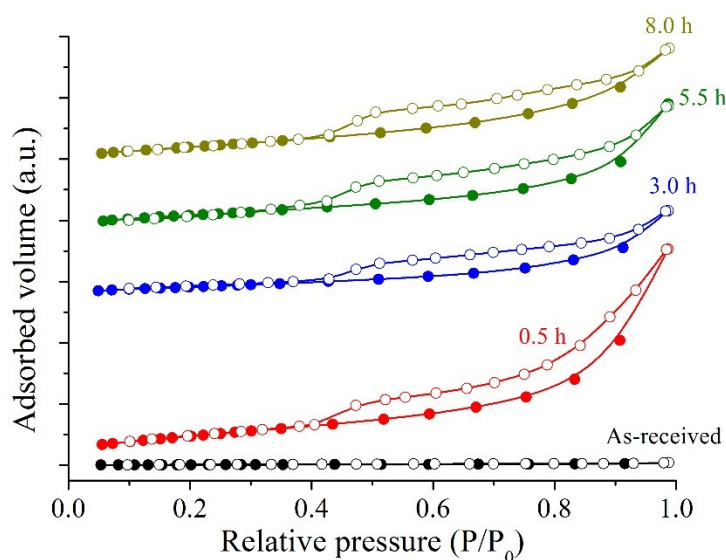
Figure 5.39 – Adsorption and desorption volume of the different leaching times of the powder

By leaching the powder, with average size between 53-106μm, and thus removing the QC phase leaving a skeletal scaffold in the particles, demonstrated in the SEM images, the total surface area is greatly increased, as shown in Figure 5.40. Beyond 0.5h of leaching most pores created in the material have, on average, 3.6nm of diameter, putting them in the mesopore range.

As to the 0.5h leached powder although it also has most of its pores in the same diameter as the longer leached samples, the quantity of these small sized pores is smaller, with a larger distribution of these pore up to 160nm of diameter, while for the longer leaching times most pores have a size smaller than 120nm.

Considering the results of XRD and BET, the 3.0h leaching time was chosen for the catalysis experiments, as the pore size and distribution does not change significantly above this leaching duration. Additionally, from the XRD analysis comparatively the 3.0h sample is the one that does not display the formation of Fe on its surface therefore being preferable to the other conditions.
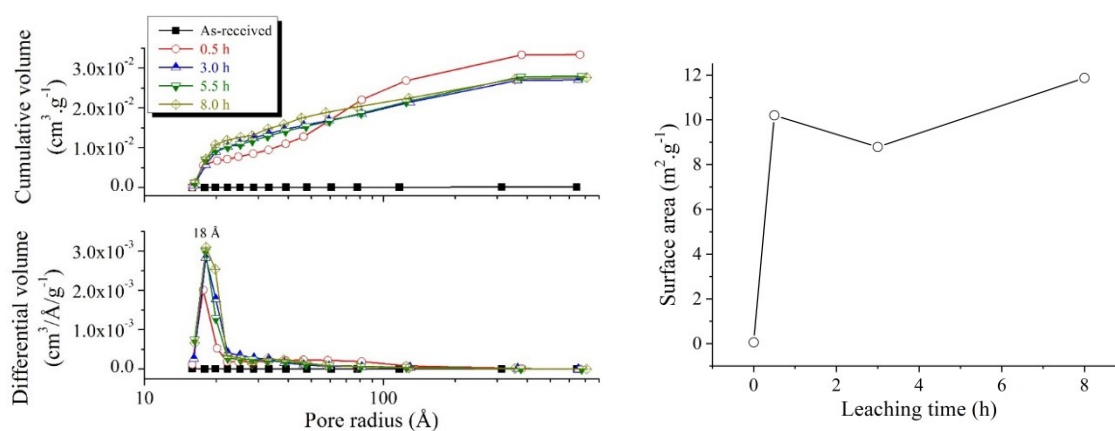
Figure 5.40 – Pore size of the different leaching times of the powder and surface area change with leaching time.

5.4. Transmission electron microscopy (TEM)

Figure 5.41 shows three particles analysed by TEM, with their respective chemical composition analysed by EDS. C and Ni were identified in all the measurements but their values are not displayed in the images. They are both artifacts from the sample preparation procedure. All particle showed high Cu and O contents. Additionally, a SAED pattern taken from the third particle confirms that the phase is indeed the τ-AlCu(Fe), which is the phase

with the skeletal morphology shown in the SEM micrographs. This phase is Cu-rich and would provide adequate sites for capturing and decomposing the Congo Red molecules due to the catalytical properties of Cu [71,74–76]. Since the catalytical properties depends on the oxidation state of the metallic atoms, these Cu-rich particles were analysed using EELS and the results will be shown in the sequence.
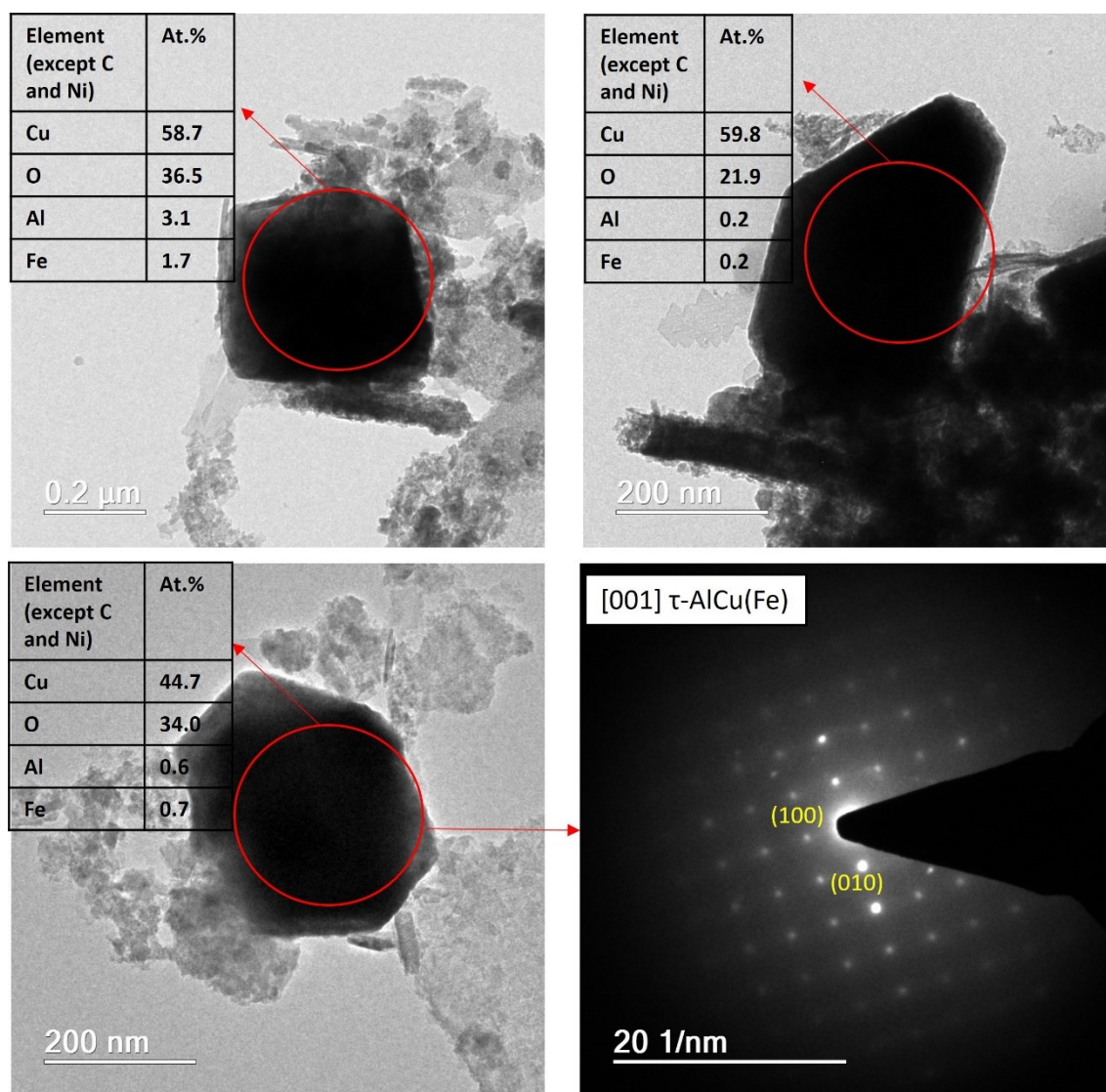
Figure 5.41 – TEM micrographs showing three different particles and their high Cu and oxygen content (measured by EDS). Only the Cu, O, Al and Fe content measured were displayed in the images. Additionally a SAED pattern taken from the bottom left particle, confirms that the particle is from the τ-AlCu(Fe) phase.

The EELS filtered signal is displayed in Figure 5.42, and shows that the measured profile approximates to that available in the literature for both, CuO and Cu_2O [77,78]. Comparing both patterns, together with the XRD results, it can be inferred that the prevalent Cu ion present in the particles is Cu^+ which is known to be a catalyst for oxidation of organic

compounds such as Congo Red and Methyl Orange, both dyes with azo groups present in their structures [71,72,74,79,80].
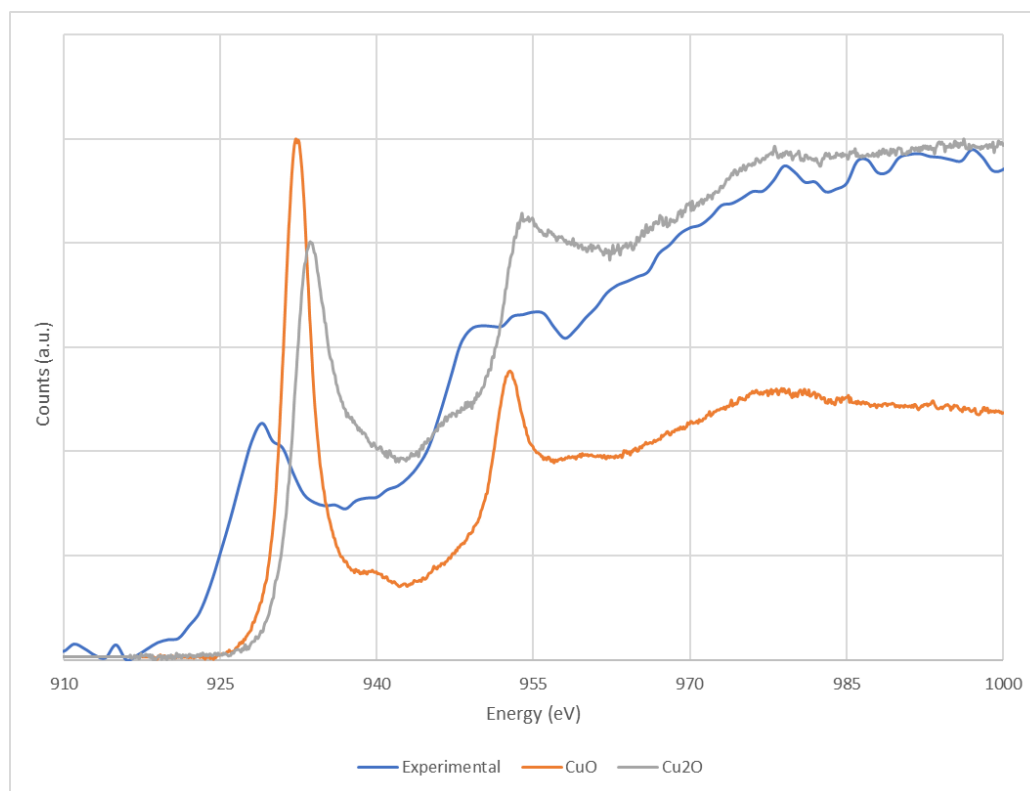
Figure 5.42 – Comparison of the measured EELS for the sample, against reference patterns *[78]*.

5.5. Catalysis

The calibration curve was measured prior to the catalysis experiments, given that it is needed to assess the degradation progress during the above-mentioned experiments. The curve is presented in Figure 5.43, the data points were used in fitting a linear equation, that stablishes the relation between CR concentration and the respective absorbance, which was later used to calculate the CR concentration after a given time in the experiments.
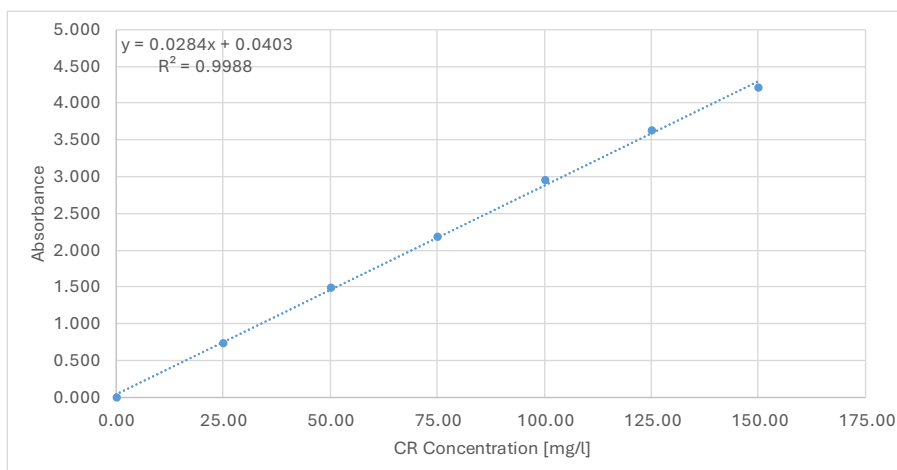
Figure 5.43 – Calibration curve for CR

In the catalysis experiments the measured absorbance of the samples were grouped in the graphics in Figure 5.44. For both CR concentration experiments, as the reaction time increases the absorbance peak intensities measured decay. In the reference literature the max peak in the CR spectrum is located at 497nm [81] and is caused by the π–π* transition of the azo bond (–N=N–), while the peak at in the 340nm vicinity originates from the naphthalene rings in the dye. To calculate the concentration at a given reaction time the absorbance in the 497nm wavelength was used, as it demonstrates the elimination of the azo bonds.
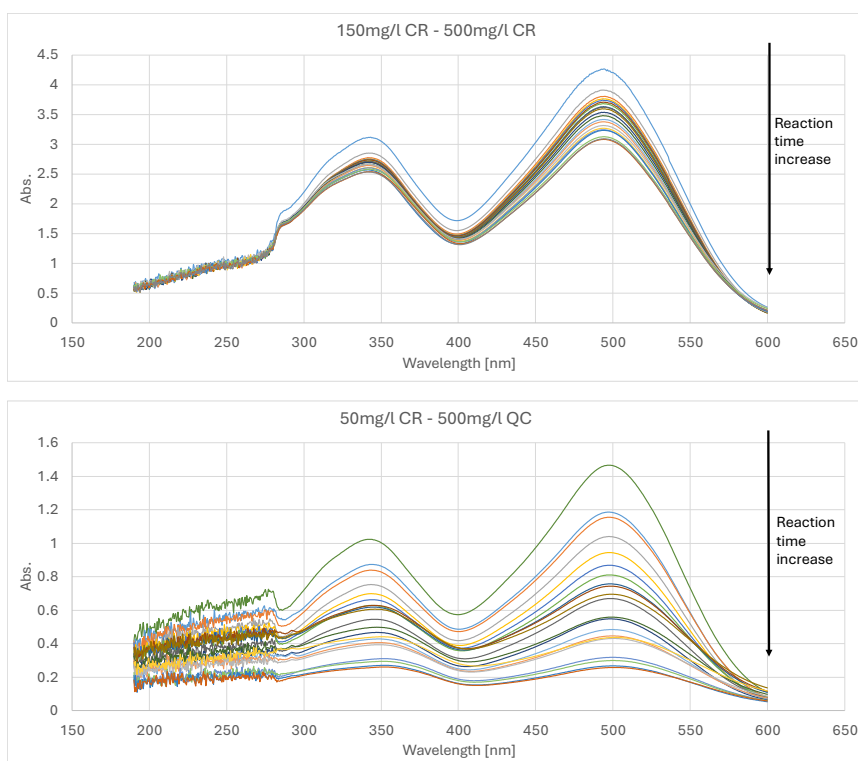
Figure 5.44 – Above: CR catalytic experiment with 150mg/l concentration. Below: CR catalytic experiment with 50mg/l concentration.

While in Figure 5.44 we have all the spectra ranging from 0 to 300 minutes, in Figure 5.45 only some selected times are shown: 0, 100, 200, 300 and 7200 minutes; the maximum reaction time evaluated for both cases was 7200 minutes. In these longer duration of the test in the 497nm wavelength there is a further drop compared to the 300 minutes absorbance value. However, there is a new peak at 369nm in the 150mg/l test and at 368nm in the 50mg/l test, virtually the same point. The origin of this peak is attributed to disubstituted benzene derivatives and naphthalene derivatives that originate through the degradation reaction by Malwal [82].
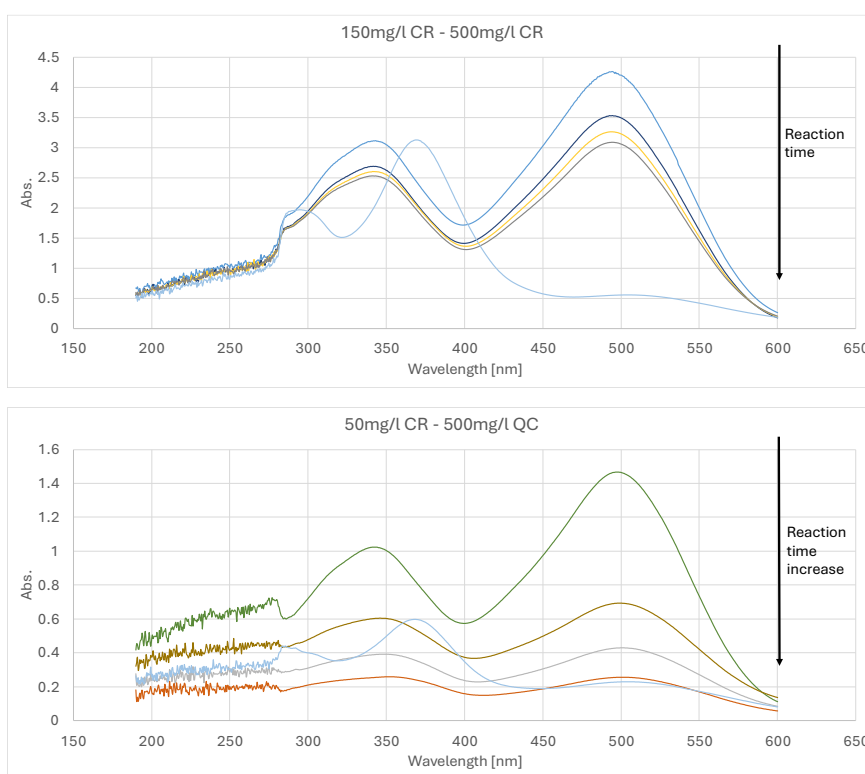
Figure 5.45 – Above: CR catalytic experiment with 150mg/l concentration. Below: CR catalytic experiment with 50mg/l concentration. Both cases limited to the following times: 0, 100, 200, 300 and 7200 minutes of reaction.

The concentration decay of CR, in both setups is shown in Figure 5.46. For both cases there is a clear drop in the CR concentration, most likely arising from the adsorption of CR into the AlCuFe particles.
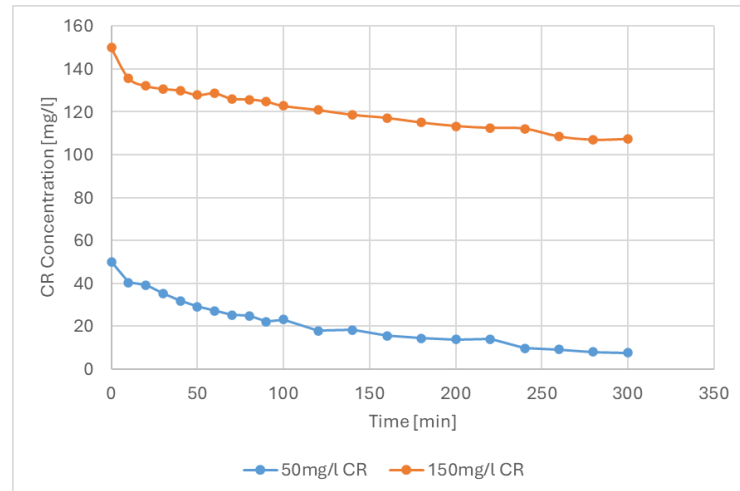
Figure 5.46 – Variation of the measured concentration of CR in both experiments.

As to degradation of CR, the comparison in both setups is shown in Figure 5.47, from the collected date the lower concentration solution is quickly degraded by the present particles in comparison to the higher concentration one, with the former reaching up to 84.74% and the latter 28.53% in the 300 minutes time spam shown. The same jump in the first minutes of reaction in both CR concentration experiments can also be noted here.

Regarding the longer reaction time of 7200 minutes the total degradation reached is of 87.92% for the 150mg/l concentration run and of 86,78% for the 50mg/l concentration, this shows that a degradation limit exists for the total degradation of CR in the current experimental setup.
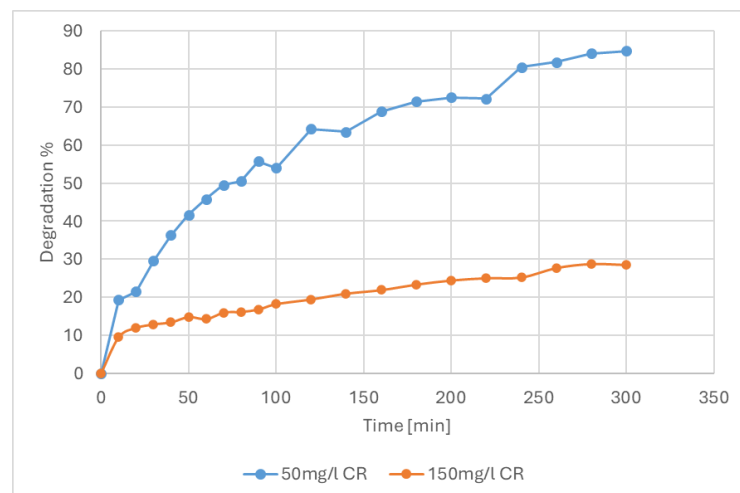
Figure 5.47 – Degradation of CR over time for both start concentrations – 50 and 160mg/l.

Fitting the linearized concentration allows to identify the rate constant for both reactions, 0.0014 and 0.0068min^{-1}, for 150mg/l and 50mg/l respectively, shown in Figure 5.48

and Figure 5.49. The slower drop verified in the higher concentration of CR test, is probably due to the particles being overwhelmed by CR, with a higher availability of CR than that the number of particles can degrade, possibly due to the limitation of access to the active sites in the particles.
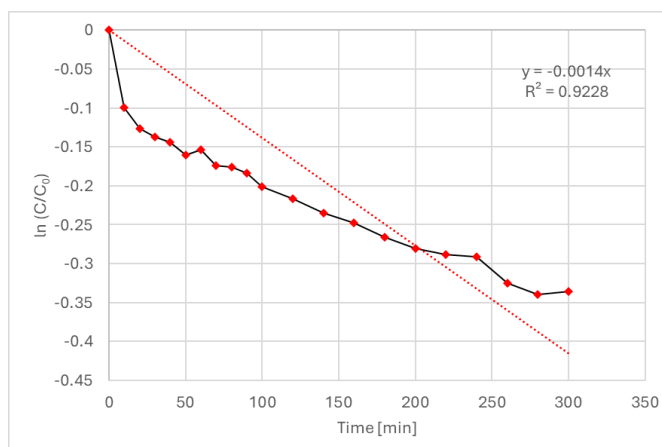
Figure 5.48 – Plot of $\ln(C/C_0)$ against the reaction time for 150mg/l concentration of CR.
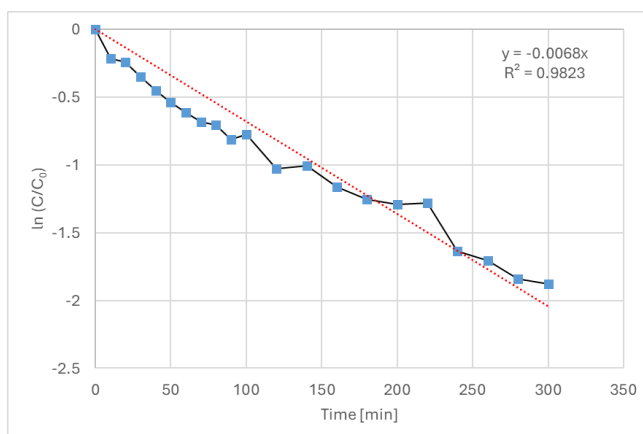
Figure 5.49 – Plot of $\ln(C/C_0)$ against the reaction time for 50mg/l concentration of CR.

On the other hand, the lower concentration of CR, Figure 5.49, shows a higher degradation rate, possibly in a lower concentration of CR there was enough space in the active sites to allow for a faster degradation of the azo bonds, associated to the 497nm characteristic peak. However, no peaks related to the disubstituted benzene derivatives and naphthalene derivatives, appeared in the 300 minutes, solely in the longer reaction times showing that the degradation reaction processes itself in a multistep process.

6   CONCLUSIONS

In this work, leached powder of atomized Al-Cu-Fe QC was successfully produced. The leached powder was then milled to increase the total area of active sites. The non-leached powder shows characteristic peaks for the quasicrystal, while after leaching the quasicrystalline alloy is mostly removed, leaving mostly of the τ-AlCu(Fe) phase, an Al-Cu rich phase with higher mesopores volume and a skeletal morphology, providing numerous sites of Cu particles. Through EELS analysis it was possible to identify the presence of both CuO and Cu_2O in the leached powder which is a known catalyst due to the presence of Cu^{2+} and Cu^+. The milled and leached powder was evaluated in respect to its catalytic properties in two different concentrations of Congo Red, 50 and 150mg/l. The catalytic capacity of the leached powder was demonstrated for both concentrations, with the breakage of the azo bond (–N=N–), shown by intensity reduction of the 497nm peak in the CR UV-Vis spectrum. It was also shown that longer reaction times further degrades the bonds present in the CR with a peak on the 370nm vicinity which can be associated to disubstituted benzene derivatives and naphthalene derivatives. The use of leached Al-Cu-Fe QC powder was demonstrated to be a viable catalyst for Congo Red degradation.

6   CONCLUSÃO

Neste trabalho, foi produzido com sucesso o pó lixiviado de Al-Cu-Fe QC atomizado. O pó lixiviado foi então moído para aumentar a área total de locais ativos. O pó não-lixiviado apresenta picos característicos para o quasicristal, enquanto que após a lixiviação a liga quasicristalina é em sua maioria removida, deixando principalmente a fase τ-AlCu(Fe), uma fase rica em Al-Cu com maior volume de mesoporos e uma morfologia esqueletal, fornecendo inúmeros locais de partículas de Cu. Através da análise EELS foi possível identificar a presença de CuO e Cu_2O no pó lixiviado que é um catalisador conhecido devido à presença de Cu^{2+} e Cu_+. O pó moído e lixiviado foi avaliado em relação às suas propriedades catalíticas em duas concentrações diferentes de Vermelho Congo, 50 e 150mg/l. A capacidade catalítica do pó lixiviado foi demonstrada para ambas as concentrações, com a quebra da ligação azo (–N=N–), demonstrada pela redução da intensidade do pico de 497nm no espectro CR UV-Vis. Também foi demonstrado que tempos de reação mais longos degradam ainda mais as ligações presentes no CR com um pico na vizinhança de 370nm que pode ser associado a derivados de benzeno e naftaleno. O uso do pó lixiviado de Al-Cu-Fe QC foi demonstrado como sendo um catalisador viável para a degradação do Congo Red.

7 SUGGESTIONS FOR FUTURE WORKS

- Further milling of the Al-Cu-Fe powder, to increase its surface area.

- Evaluate the degradation effect on Congo Red of the presence of UV and solar light.

- Perform gas chromatography-mass spectrometry of the remaining catalysed solution aiming to identify the produced chemical species after degradation.

- Vary the leaching intensity to evaluate the oxidation state of the remaining phases.

- Evaluate the remaining liquid after leaching as to the prevalent chemical species removed by the process.

- Evaluate the biotoxicity of the remaining solution after catalysis, using algae and bacteria as indicators.

8 REFERENCES

[1]   D. Shechtman, I. Blech, D. Gratias, J.W. Cahn, Metallic Phase with Long-Range Orientational Order and No Translational Symmetry, Phys. Rev. Lett. 53 (1984) 1951–1953. https://doi.org/10.1103/PhysRevLett.53.1951.

[2]   L. Bindi, P.J. Steinhardt, N. Yao, P.J. Lu, Icosahedrite, $Al_{63}Cu_{24}Fe_{13}$, the first natural quasicrystal, Am. Mineral. 96 (2011) 928–931. https://doi.org/10.2138/am.2011.3758.

[3]   L. Bindi, N. Yao, C. Lin, L.S. Hollister, C.L. Andronicos, V.V. Distler, M.P. Eddy, A. Kostin, V. Kryachko, G.J. MacPherson, W.M. Steinhardt, M. Yudovskaya, P.J. Steinhardt, Natural quasicrystal with decagonal symmetry, Sci. Rep. 5 (2015) 9111. https://doi.org/10.1038/srep09111.

[4]   S.S. Mishra, T.P. Yadav, S.P. Singh, A.K. Singh, M.A. Shaz, N.K. Mukhopadhyay, O.N. Srivastava, Evolution of porous structure on Al–Cu–Fe quasicrystalline alloy surface and its catalytic activities, J. Alloys Compd. 834 (2020) 155162. https://doi.org/10.1016/j.jallcom.2020.155162.

[5]   F. Hoffmann, Introduction to Crystallography, Springer International Publishing, Cham, 2020. https://doi.org/10.1007/978-3-030-35110-6.

[6]   W. Borchardt-Ott, Crystallography, 3rd ed, Springer, Germany, 2011.

[7]   M. De Graef, M.E. McHenry, Structure of materials: an introduction to crystallography, diffraction, and symmetry, Second edition, fully revised and updated, Cambridge University Press, New York, 2012.

[8]   D. Levine, P.J. Steinhardt, Quasicrystals. I. Definition and structure, Phys. Rev. B. 34 (1986) 596–616. https://doi.org/10.1103/PhysRevB.34.596.

[9]   R. Penrose, The role of aesthetics in pure and applied mathematical research, Bull Inst Math Appl. 10 (1974) 266–271.

[10]   D. Levine, P.J. Steinhardt, Quasicrystals: A New Class of Ordered Structures, Phys. Rev. Lett. 53 (1984) 2477–2480. https://doi.org/10.1103/PhysRevLett.53.2477.

[11]   U. Grimm, Aperiodic crystals and beyond, Acta Crystallogr. Sect. B Struct. Sci. Cryst. Eng. Mater. 71 (2015) 258–274. https://doi.org/10.1107/S2052520615008409.

[12]   V. Elser, Indexing problems in quasicrystal diffraction, Phys. Rev. B. 32 (1985) 4892–4898. https://doi.org/10.1103/PhysRevB.32.4892.

[13]   F. Zupanič, T. Bončina, A. Križman, W. Grogger, C. Gspan, B. Markoli, S. Spaić, Quasicrystalline phase in melt-spun Al–Mn–Be ribbons, J. Alloys Compd. 452 (2008) 343–347. https://doi.org/10.1016/j.jallcom.2006.11.041.

[14]   L. Bindi, P.J. Steinhardt, N. Yao, P.J. Lu, Natural Quasicrystals, Science. 324 (2009) 1306–1309. https://doi.org/10.1126/science.1170827.

[15]   L. Bindi, W. Kolb, G.N. Eby, P.D. Asimow, T.C. Wallace, P.J. Steinhardt, Accidental synthesis of a previously unknown quasicrystal in the first atomic bomb test, Proc. Natl. Acad. Sci. 118 (2021) e2101350118. https://doi.org/10.1073/pnas.2101350118.

[16]   S. Fischer, A. Exner, K. Zielske, J. Perlich, S. Deloudi, W. Steurer, P. Lindner, S. Förster, Colloidal quasicrystals with 12-fold and 18-fold diffraction symmetry, Proc. Natl. Acad. Sci. 108 (2011) 1810–1814. https://doi.org/10.1073/pnas.1008695108.

[17]   W. Steurer, S. Deloudi, Fascinating quasicrystals, Acta Crystallogr. A. 64 (2008) 1–11. https://doi.org/10.1107/S0108767307038627.

[18]   W. Steurer, Twenty years of structure research on quasicrystals. Part I. Pentagonal, octagonal, decagonal and dodecagonal quasicrystals, Z. Für Krist. - Cryst. Mater. 219 (2004) 391–446. https://doi.org/10.1524/zkri.219.7.391.35643.

[19]   W. Steurer, Quasicrystals: What do we know? What do we want to know? What can we know?, Acta Crystallogr. Sect. Found. Adv. 74 (2018) 1–11. https://doi.org/10.1107/S2053273317016540.

[20]   K.F. Kelton, Quasicrystals: structure and stability, Int. Mater. Rev. 38 (1993) 105–137. https://doi.org/10.1179/imr.1993.38.3.105.

[21]   C. Janot, The Properties and Applications of Quasicrystals, Europhys. News. 27 (1996) 60–64. https://doi.org/10.1051/epn/19962702060.

[22]   E. Huttunen-Saarivirta, Microstructure, fabrication and properties of quasicrystalline Al–Cu–Fe alloys: a review, J. Alloys Compd. 363 (2004) 154–178. https://doi.org/10.1016/S0925-8388(03)00445-6.

[23]   C. Janot, Quasicrystals: a primer, Second edition, Oxford University Press, Oxford, 2012.

[24]   J.-M. Dubois, Useful quasicrystals, World Scientific, Hackensack, NJ, 2005.

[25]   O.D. Neikov, ed., Handbook of non-ferrous metal powders: technologies and applications, 1. ed, Elsevier, Amsterdam, 2009.

[26]   J.-M. Dubois, New prospects from potential applications of quasicrystalline materials, Mater. Sci. Eng. A. 294–296 (2000) 4–9. https://doi.org/10.1016/S0921-5093(00)01305-8.

[27]   J.-M. Dubois, The applied physics of quasicrystals, Phys. Scr. T49A (1993) 17–23. https://doi.org/10.1088/0031-8949/1993/T49A/002.

[28]   J.-M. Dubois, Properties- and applications of quasicrystals and complex metallic alloys, Chem. Soc. Rev. 41 (2012) 6760. https://doi.org/10.1039/c2cs35110b.

[29]   J.-M. Dubois, S.S. Kang, Y. Massiani, Application of quasicrystalline alloys to surface coating of soft metals, J. Non-Cryst. Solids. 153–154 (1993) 443–445. https://doi.org/10.1016/0022-3093(93)90392-B.

[30]   G. Laplanche, J. Bonneville, A. Joulain, V. Gauthier-Brunet, S. Dubois, Plasticity of the ω-Al_7Cu_2Fe phase, J. Alloys Compd. 665 (2016) 144–151. https://doi.org/10.1016/j.jallcom.2015.12.161.

[31]   G. Laplanche, J. Bonneville, A. Joulain, V. Gauthier-Brunet, S. Dubois, Mechanical properties of Al–Cu–Fe quasicrystalline and crystalline phases: An analogy, Intermetallics. 50 (2014) 54–58. https://doi.org/10.1016/j.intermet.2014.02.004.

[32]   E. Fleury, Y.-C. Kim, J.-S. Kim, D.-H. Kim, W.T. Kim, H.-S. Ahn, S.-M. Lee, Comparative study of the tribological behavior of thermal sprayed quasicrystalline coating layers, J. Alloys Compd. 342 (2002) 321–325. https://doi.org/10.1016/S0925-8388(02)00246-3.

[33]   D. Lu, J.P. Celis, S. Kenzari, V. Fournée, D.B. Zhou, Tribological behavior of aluminum matrix composites containing complex metallic alloys AlCuFeB or AlCuFeCr particles, Wear. 270 (2011) 528–534. https://doi.org/10.1016/j.wear.2011.01.007.

[34]   X. Guo, J. Chen, H. Yu, H. Liao, C. Coddet, A study on the microstructure and tribological behavior of cold-sprayed metal matrix composites reinforced by particulate

quasicrystal, Surf. Coat. Technol. 268 (2015) 94–98.
https://doi.org/10.1016/j.surfcoat.2014.05.062.

[35]   M. Sales, A. Merstallinger, A.I. Ustinov, S.S. Polishchuk, T.V. Melnichenko, Effect of
the addition of crystalline β-phase in Al–Cu–Fe quasicrystalline coatings on their tribological
properties, Surf. Coat. Technol. 201 (2007) 6206–6211.
https://doi.org/10.1016/j.surfcoat.2006.11.014.

[36]   C. Zhou, F. Cai, J. Kong, S. Gong, H. Xu, A study on the tribological properties of
low-pressure plasma-sprayed Al–Cu–Fe–Cr quasicrystalline coating on titanium alloy, Surf.
Coat. Technol. 187 (2004) 225–229. https://doi.org/10.1016/j.surfcoat.2004.03.013.

[37]   R.P. Matthews, C.I. Lang, D. Shechtman, Sliding wear of quasicrystalline coatings,
Tribol. Lett. 7 (1999) 179–181. https://doi.org/10.1023/A:1019185707264.

[38]   W. Wolf, C. Bolfarini, C.S. Kiminami, W.J. Botta, Recent developments on
fabrication of Al-matrix composites reinforced with quasicrystals: From metastable to
conventional processing, J. Mater. Res. 36 (2021) 281–297. https://doi.org/10.1557/s43578-
020-00083-4.

[39]   M. Yoshimura, A.P. Tsai, Quasicrystal application on catalyst, J. Alloys Compd. 342
(2002) 451–454. https://doi.org/10.1016/S0925-8388(02)00274-8.

[40]   B. Ngoc, Quasicrystal derived catalyst for steam reforming of methanol, Int. J.
Hydrog. Energy. 33 (2008) 1000–1007. https://doi.org/10.1016/j.ijhydene.2007.11.019.

[41]   S. Kameoka, T. Tanabe, A.P. Tsai, Al–Cu–Fe quasicrystals for steam reforming of
methanol: a new form of copper catalysts, Catal. Today. 93–95 (2004) 23–26.
https://doi.org/10.1016/j.cattod.2004.05.010.

[42]   A.P. Tsai, M. Yoshimura, Highly active quasicrystalline Al-Cu-Fe catalyst for steam
reforming of methanol, Appl. Catal. Gen. 214 (2001) 237–241.
https://doi.org/10.1016/S0926-860X(01)00500-2.

[43]   T. Tanabe, S. Kameoka, A.P. Tsai, A novel catalyst fabricated from Al–Cu–Fe
quasicrystal for steam reforming of methanol, Catal. Today. 111 (2006) 153–157.
https://doi.org/10.1016/j.cattod.2005.11.003.

[44]   T. Tanabe, S. Kameoka, F. Sato, M. Terauchi, A. Pang Tsai, Cross-section TEM investigation of quasicrystalline catalysts prepared by aqueous NaOH leaching, Philos. Mag. 87 (2007) 3103–3108. https://doi.org/10.1080/14786430701365017.

[45]   M. Lowe, T.P. Yadav, V. Fournée, J. Ledieu, R. McGrath, H.R. Sharma, Influence of leaching on surface composition, microstructure, and valence band of single grain icosahedral Al-Cu-Fe quasicrystal, J. Chem. Phys. 142 (2015) 094703. https://doi.org/10.1063/1.4913567.

[46]   Hamed Bateni, Chad Able, Development of Heterogeneous Catalysts for Dehydration of Methanol to Dimethyl Ether: A Review, Catal. Ind. 11 (2019) 7–33. https://doi.org/10.1134/S2070050419010045.

[47]   C.J. Jenks, P.A. Thiel, Comments on quasicrystals and their potential use as catalysts, J. Mol. Catal. Chem. 131 (1998) 301–306. https://doi.org/10.1016/S1381-1169(97)00272-0.

[48]   B.P. Ngoc, C. Geantet, J.A. Dalmon, M. Aouine, G. Bergeret, P. Delichere, S. Raffy, S. Marlin, Quasicrystalline Structures as Catalyst Precursors for Hydrogenation Reactions, Catal. Lett. 131 (2009) 59–69. https://doi.org/10.1007/s10562-009-0018-8.

[49]   S.S. Mishra, T.P. Yadav, N.K. Mukhopadhyay, O.N. Srivastava, Synthesis of fine skeletal structure on Al–Cu–Co decagonal quasicrystals for hydrogen production through steam reforming of methanol, Int. J. Hydrog. Energy. 45 (2020) 24491–24501. https://doi.org/10.1016/j.ijhydene.2020.06.216.

[50]   S.K. Pandey, A. Bhatnagar, S.S. Mishra, T.P. Yadav, M.A. Shaz, O.N. Srivastava, Curious Catalytic Characteristics of Al–Cu–Fe Quasicrystal for De/Rehydrogenation of MgH_2, J. Phys. Chem. C. 121 (2017) 24936–24944. https://doi.org/10.1021/acs.jpcc.7b07336.

[51]   A.-P. Tsai, A. Inoue, T. Masumoto, Icosahedral, Decagonal and Amorphous Phases in Al-Cu-M (M=Transition Metal) Systems, Mater. Trans. JIM. 30 (1989) 666–676. https://doi.org/10.2320/matertrans1989.30.666.

[52]   A.-P. Tsai, A. Inoue, T. Masumoto, A Stable Quasicrystal in Al-Cu-Fe System, Jpn. J. Appl. Phys. 26 (1987) L1505–L1507. https://doi.org/10.1143/JJAP.26.L1505.

[53]   F. Faudot, A. Quivy, Y. Calvayrac, D. Gratias, M. Harmelin, About the Al-Cu-Fe icosahedral phase formation, Mater. Sci. Eng. A. 133 (1991) 383–387. https://doi.org/10.1016/0921-5093(91)90093-3.

[54]   Ullmann's Encyclopedia of Industrial Chemistry, 1st ed., Wiley, 2000. https://doi.org/10.1002/14356007.

[55]   U. Hanefeld, L. Lefferts, eds., Catalysis: an integrated textbook for students, Wiley-VCH, Weinheim, 2018.

[56]   M. Ismail, K. Akhtar, M.I. Khan, T. Kamal, M.A. Khan, A. M. Asiri, J. Seo, S.B. Khan, Pollution, Toxicity and Carcinogenicity of Organic Dyes and their Catalytic Bio-Remediation, Curr. Pharm. Des. 25 (2019) 3645–3663. https://doi.org/10.2174/1381612825666191021142026.

[57]   M.A. Brown, S.C. De Vito, Predicting azo dye toxicity, Crit. Rev. Environ. Sci. Technol. 23 (1993) 249–324. https://doi.org/10.1080/10643389309388453.

[58]   R.A. van Santen, ed., Modern Heterogeneous Catalysis: An Introduction, Wiley-VCH Verlag GmbH & Co. KGaA, Weinheim, Germany, 2017. https://doi.org/10.1002/9783527810253.

[59]   J.C. Lindon, G.E. Tranter, D.W. Koppenaal, eds., Encyclopedia of spectroscopy and spectrometry, Third edition, Elsevier/AP, Academic Press is an imprint of Elsevier, Amsterdam ; Boston, 2017.

[60]   M. Clark, ed., Handbook of textile and industrial dyeing, Woodhead Publishing Limited, Oxford ; Philadelphia, 2011.

[61]   P. Böttiger, Verfahren zur Darstellung von Azofarbstoffen durch Kombination von Tetrazodiphenylsalzen mit α- und β-Naphtylamin oder deren Mono- und Disulfosäuren, DE28753C, 1884.

[62]   M. Rochkind, S. Pasternak, Y. Paz, Using Dyes for Evaluating Photocatalytic Properties: A Critical Review, Molecules. 20 (2014) 88–110. https://doi.org/10.3390/molecules20010088.

[63]   V.S. Kirankumar, B. Hardik, S. Sumathi, Photocatalytic degradation of congo red using copper substituted cobalt ferrite, IOP Conf. Ser. Mater. Sci. Eng. 263 (2017) 022027. https://doi.org/10.1088/1757-899X/263/2/022027.

[64]   U.O. Bhagwat, J.J. Wu, A.M. Asiri, S. Anandan, Photocatalytic Degradation of Congo Red Using $PbTiO_3$ Nanorods Synthesized via a Sonochemical Approach, ChemistrySelect. 3 (2018) 11851–11858. https://doi.org/10.1002/slct.201802303.

[65]   Y. Dong, Z. Wang, X. Yang, M. Zhu, R. Chen, B. Lu, H. Liu, Adsorption and degradation of Congo red on a jarosite-type compound, RSC Adv. 6 (2016) 102972–102978. https://doi.org/10.1039/C6RA19125H.

[66]   L. Devi, S. Kumar, K. Reddy, Photo fenton like process $Fe^{3+}/(NH_4)_2S_2O_8$/UV for the degradation of Di azo dye congo red using low iron concentration, Open Chem. 7 (2009) 468–477. https://doi.org/10.2478/s11532-009-0036-9.

[67]   S. Argote-Fuentes, R. Feria-Reyes, E. Ramos-Ramírez, N. Gutiérrez-Ortega, G. Cruz-Jiménez, Photoelectrocatalytic Degradation of Congo Red Dye with Activated Hydrotalcites and Copper Anode, Catalysts. 11 (2021) 211. https://doi.org/10.3390/catal11020211.

[68]   V.A. Sakkas, Md.A. Islam, C. Stalikas, T.A. Albanis, Photocatalytic degradation using design of experiments: A review and example of the Congo red degradation, J. Hazard. Mater. 175 (2010) 33–44. https://doi.org/10.1016/j.jhazmat.2009.10.050.

[69]   A. Sadollahkhani, Z. Hussain Ibupoto, S. Elhag, O. Nur, M. Willander, Photocatalytic properties of different morphologies of CuO for the degradation of Congo red organic dye, Ceram. Int. 40 (2014) 11311–11317. https://doi.org/10.1016/j.ceramint.2014.03.132.

[70]   L.-J. Han, Y.-J. Kong, T.-J. Yan, L.-T. Fan, Q. Zhang, H.-J. Zhao, H.-G. Zheng, A new five-coordinated copper compound for efficient degradation of methyl orange and Congo red in the absence of UV–visible radiation, Dalton Trans. 45 (2016) 18566–18571. https://doi.org/10.1039/C6DT03273G.

[71]   Y. Yue, P. Zhang, W. Wang, Y. Cai, F. Tan, X. Wang, X. Qiao, P.K. Wong, Enhanced dark adsorption and visible-light-driven photocatalytic properties of narrower-band-gap Cu_2S decorated Cu_2O nanocomposites for efficient removal of organic pollutants, J. Hazard. Mater. 384 (2020) 121302. https://doi.org/10.1016/j.jhazmat.2019.121302.

[72]   J. Shu, Z. Wang, Y. Huang, N. Huang, C. Ren, W. Zhang, Adsorption removal of Congo red from aqueous solution by polyhedral Cu_2O nanoparticles: Kinetics, isotherms, thermodynamics and mechanism analysis, J. Alloys Compd. 633 (2015) 338–346. https://doi.org/10.1016/j.jallcom.2015.02.048.

[73]   S.S. Mishra, T.P. Yadav, N.K. Mukhopadhyay, O.N. Srivastava, Synthesis of fine skeletal structure on Al–Cu–Co decagonal quasicrystals for hydrogen production through steam reforming of methanol, Int. J. Hydrog. Energy. 45 (2020) 24491–24501. https://doi.org/10.1016/j.ijhydene.2020.06.216.

[74]   J.-Y. Ho, M.H. Huang, Synthesis of Submicrometer-Sized Cu_2O Crystals with Morphological Evolution from Cubic to Hexapod Structures and Their Comparative Photocatalytic Activity, J. Phys. Chem. C. 113 (2009) 14159–14164. https://doi.org/10.1021/jp903928p.

[75]   Z. Zheng, B. Huang, Z. Wang, M. Guo, X. Qin, X. Zhang, P. Wang, Y. Dai, Crystal Faces of Cu_2O and Their Stabilities in Photocatalytic Reactions, J. Phys. Chem. C. 113 (2009) 14448–14453. https://doi.org/10.1021/jp904198d.

[76]   Z. Li, X. Chen, M. Wang, X. Zhang, L. Liao, T. Fang, B. Li, Photocatalytic degradation of Congo Red by using the $Cu_2O/\alpha\text{-}Fe_2O_3$ composite catalyst, DESALINATION WATER Treat. 215 (2021) 222–231. https://doi.org/10.5004/dwt.2021.26799.

[77]   P. Ewels, T. Sikora, V. Serin, C.P. Ewels, L. Lajaunie, A Complete Overhaul of the Electron Energy-Loss Spectroscopy and X-Ray Absorption Spectroscopy Database: eelsdb.eu, Microsc. Microanal. 22 (2016) 717–724. https://doi.org/10.1017/S1431927616000179.

[78]   J.P. Ngantcha, M. Gerland, Y. Kihn, A. Rivière, Correlation between microstructure and mechanical spectroscopy of a $Cu\text{-}Cu_2O$ alloy between 290 K and 873 K, Eur. Phys. J. Appl. Phys. 29 (2005) 83–89. https://doi.org/10.1051/epjap:2004200.

[79]   L. Chen, S. Shet, H. Tang, H. Wang, T. Deutsch, Y. Yan, J. Turner, M. Al-Jassim, Electrochemical deposition of copper oxide nanowires for photoelectrochemical applications, J. Mater. Chem. 20 (2010) 6962. https://doi.org/10.1039/c0jm01228a.

[80]   X. Zhang, Y. Zhang, D. Wang, F. Qu, Investigation of Adsorption Behavior of Cu_2O Submicro-Octahedra towards Congo Red, J. Nanomater. 2014 (2014) 1–6. https://doi.org/10.1155/2014/619239.

[81]   R.W. Sabnis, Handbook of biological dyes and stains: synthesis and industrial applications, Wiley, Hoboken, N.J, 2010.

[82]   D. Malwal, P. Gopinath, Enhanced photocatalytic activity of hierarchical three dimensional metal oxide@CuO nanostructures towards the degradation of Congo red dye under solar radiation, Catal. Sci. Technol. 6 (2016) 4458–4472. https://doi.org/10.1039/C6CY00128A.